Earth-Abundant Zinc-IV-Nitride Semiconductors

Thesis by
Naomi Cristina Coronel

In Partial Fulfillment of the Requirements
for the Degree of

Doctor of Philosophy

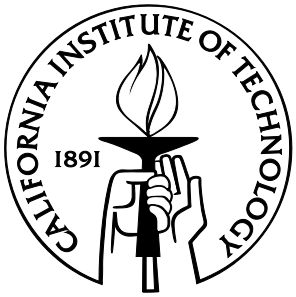

California Institute of Technology
Pasadena, California

2016

(Defended June 15, 2015)

Acknowledgements

I would like to first thank Prof. Harry Atwater for providing an opportunity to research such a challenging and interesting subject, and for his encouragement and optimism throughout. I would also like to thank Prof. Julia Greer, Prof. Kaushik Bhattacharya, Prof. Austin Minnich, and Prof. Brent Fultz for sharing their insights and perspectives as members of my thesis and candidacy committees. I thank Carol Garland and Ali Ghaffari for giving their time and energy to teach. I am grateful to have had the support of Lise Lahourcade and Amanda Shing in our joint pursuit of zinc-IV-nitride materials, and I am also thankful for the camaraderie of Yulia Tolstova, Samantha Wilson, Jeff Bosco, Greg Kimball, and Davis Darvish in investigating earth-abundant semiconductors. Many thanks to everyone in the Atwater group who contributed to this research in ways big and small, especially to Tiffany Kimoto and Jennifer Blankenship for their continual support and assistance. Finally, this work would not be possible without funding and support from the DOE and Dow Chemical Company.

Naomi C. Coronel

June 2015

Pasadena, CA

Abstract

This investigation is motivated by the need for new visible frequency direct bandgap semiconductor materials that are abundant and low-cost to meet the increasing demand for optoelectronic devices in applications such as solid state lighting and solar energy conversion. Proposed here is the utilization of zinc-IV-nitride materials, where group IV elements include silicon, germanium, and tin, as earth-abundant alternatives to the more common III-nitrides in optoelectronic devices. These compound semiconductors were synthesized under optimized conditions using reactive radio frequency magnetron sputter deposition. Single phase $ZnSnN_2$, having limited experimental accounts in literature, is validated by identification of the wurtzite-derived crystalline structure predicted by theory through X-ray and electron diffraction studies. With the addition of germanium, bandgap tunability of $ZnSn_xGe_{1-x}N_2$ alloys is demonstrated without observation of phase separation, giving these materials a distinct advantage over $In_xGa_{1-x}N$ alloys. The accessible bandgaps range from 1.8 to 3.1 eV, which spans the majority of the visible spectrum. Electron densities, measured using the Hall effect, were found to be as high as 10^{22} cm^{-3} and indicate that the compounds are unintentionally degenerately doped. Given these high carrier concentrations, a Burstein-Moss shift is likely affecting the optical bandgap measurements. The discoveries made in this thesis suggest that with some improvements in material quality, zinc-IV-nitrides have the potential to enable cost-effective and scalable optoelectronic devices.

Contents

List of Figures

List of Tables

List of Publications

Portions of this thesis have been drawn from the following publications:

P. Narang*, S. Chen*, N. C. Coronel*, S. Gul, J. Yano, L. Wang, N. S. Lewis, and H. A. Atwater, "Band Gap Tunability in Zn(Sn,Ge)N_2 Semiconductor Alloys," Advanced Materials, vol. 26, no. 8, pp. 1235–1241, 2014.

L. Lahourcade, N. C. Coronel, K. T. Delaney, S. K. Shukla, N. A. Spaldin, and H. A. Atwater, "Structural and Optoelectronic Characterization of RF Sputtered $ZnSnN_2$," Advanced Materials, vol. 25, no. 18, pp. 2562–2566, 2013.

N. C. Coronel, L. Lahourcade, K. T. Delaney, A. M. Shing, and H. A. Atwater, "Earth-Abundant $ZnSn_xGe_{1-x}N_2$ Alloys as Potential Photovoltaic Absorber Materials," Proceedings of the 38th IEEE Photovoltaic Specialists Conference (PVSC), pp.003204-003207, 2012.

* denotes equal contribution

Chapter 1

Introduction

This thesis details the exploration of zinc-IV-nitrides, a new earth-abundant class of semiconductor materials. Investigation of new materials is more important now than ever for overcoming inherent material barriers to scalability, like cost or availability. Theory predicts that zinc-IV-nitrides are well-suited for applications in optoelectronic devices, although reports of experimental characterization are limited. The work presented here strives to fill in some of the gaps in understanding of zinc-IV-nitride semiconductors.

1.1 Motivation for Studying Earth-Abundant Semiconductors

In today's technological world, semiconductors play an increasing role in everyday life. From computer chips to solar panels, semiconductors are in demand for more advanced applications every day. As the prevalence of these materials increases, the question arises as to whether or not current semiconductors are sustainable. This is an especially important issue for industries like photovoltaics and light-emitting diodes (LEDs) because the scale of their desired implementation is so large. This motivates the study of earth-abundant semiconductors that are suitable for use in visible wavelength devices.

Many of the semiconducting materials that are widely used in current devices are composed of elements that are not abundant enough in the earth's crust to meet demand. These include compounds containing gallium, selenium, cadmium, indium, and tellurium, which precludes the majority of the materials used in high efficiency LEDs (GaN, InN) and photovoltaics (GaAs, CdTe, CIGS). Cost is also a related value that can affect the availability of certain materials. For example, the rapid adoption of ITO as a transparent conducting film used in displays has increased the cost of indium, due in part to its relative scarcity. Thus, switching over to earth-abundant materials will not only allow for large-scale deployment of devices, but could also lower their cost.

There are also other environmental benefits to earth-abundant semiconductors. Abundant elements are unlikely to be toxic to the environment as they are already present in large quantities. This can reduce the need for expensive and cumbersome encapsulation or disposal of devices, which is common for CdTe and GaAs photovoltaics.

One final requirement for semiconductors being used in optoelectronic devices is that the material must have a high conversion efficiency. A device made with the cheapest, most abundant elements will not be viable if the device is not efficient at its task. This is the reason why it is important to study new earth-abundant semiconductors in-depth to determine if they have potential for producing high efficiency devices.

1.2 Zinc-IV-Nitride Literature Review

This new system of materials is derived from III-nitrides, and is obtained by substitution of group III elements with alternating group II and group IV elements. In this work, zinc was chosen as the group II element and the group IV element is varied among silicon,

germanium, and tin. The close analogy of zinc-IV-nitrides to III-nitrides suggests the same types of applications will be possible, with the added advantage of earth-abundance.

1.2.1 Theory

One of the main reasons that zinc-IV-nitrides are so interesting is that theoretical studies suggest the optical properties are favorable for device applications. Density functional theory (DFT) was the primary method of predicting these material properties, although the selection of functional was varied in different reports.

The crystal structure of zinc-IV-nitride semiconductors is expected to be the same as in the III-nitride system, hexagonal wurtzite with space group $P6_3mc$. In $ZnSnN_2$, the energetic difference between the wurtzite- and zinc-blende-derived orderings was found to be small (Figure 1.1), suggesting that both phases could coexist under certain growth

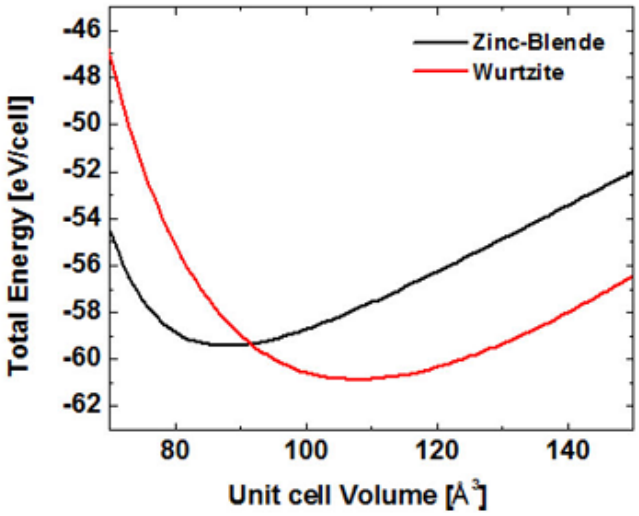

Figure 1.1. Energy of wurtzite and zinc-blende structures as a function of unit cell volume. Zinc-IV-nitrides are expected to form with the lower energy wurtzite structure. [1]

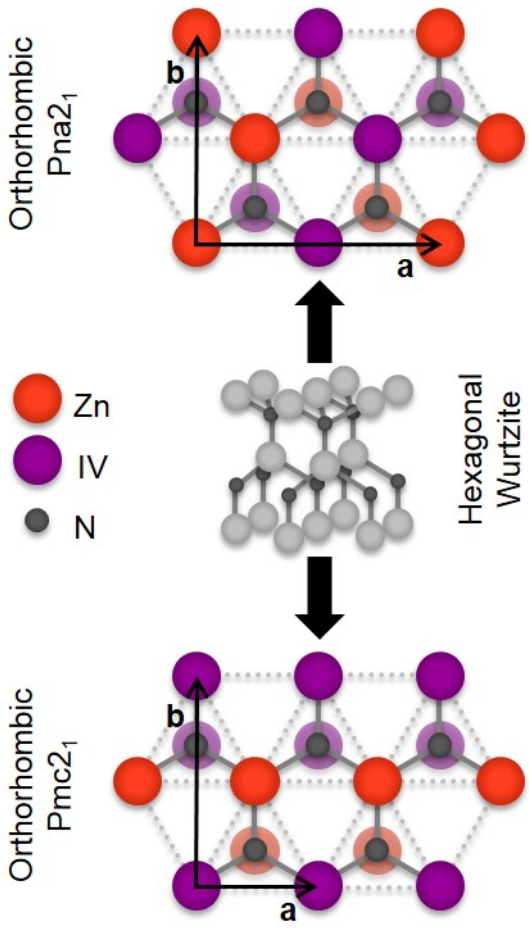

Figure 1.2. Model of the hexagonal wurtzite structure and the two possible ordering of cations in the *c*-plane. $Pna2_1$ is characterized by a zig-zag pattern of like-atoms, and $Pmc2_1$ by rows of like-atoms.

conditions [3]. However, assuming that the zinc and group IV elements are ordered in the lattice, an orthorhombic symmetry must be used to describe the unit cell instead. A model of the wurtzite structure is depicted in Figure 1.2 alongside the orthorhombic space groups that describe two different high-symmetry arrangements of the cations. Within the *c*-plane, like-elements can be arranged in rows ($Pmc2_1$) or in a zig-zag pattern ($Pna2_1$). Most of the theory work assumed the $Pna2_1$ space group for their calculations, as it is the most stable [3]. The resulting lattice parameters from the different calculations are shown in Table 1.1. It should be noted that one study assumed a monoclinic crystal system in calculating their

Table 1.1. Theoretical lattice parameters for zinc-IV-nitrides assuming an orthorhombic crystal structure. PBE0 values were converted from calculated monoclinic parameters, and are shown for comparison only. All values are reported in angstroms.

Functional	$ZnSiN_2$			$ZnGeN_2$			$ZnSnN_2$		
	a	*b*	*c*	*a*	*b*	*c*	*a*	*b*	*c*
PBE0 [4]							6.755	5.846	5.473
HSE06 [3]							6.721	5.842	5.459
GGA [5]	6.16	5.41	5.11	6.42	5.54	5.27	6.7	5.8	5.53
GGA [6]	5.279	6.307	5.071	5.535	6.513	5.269			
LDA [5]	6.08	5.27	5.02	6.38	5.45	5.22	6.59	5.7	5.41
LDA [6]	5.199	6.182	4.989	5.402	6.351	5.149			
LDA-ABINIT [7]	6.01	5.28	4.98	6.33	5.36	5.11	6.76	5.85	5.58

Table 1.2. Theoretical electronic bandgaps for zinc-IV-nitrides. Values are reported in electron volts and represent direct transitions unless otherwise noted.

Functional	$ZnSiN_2$	$ZnGeN_2$	$ZnSnN_2$
PBE0 [4]			2.09
HSE06 [3]			1.42
GGA [6]	3.32 (indirect)	1.67	
LDA [8]		2.8	
LDA [6]		2.04	
QSGW [5]	5.66	3.42	2.02
QSGW [5]	5.44 (indirect)		

lattice parameters, and the correlating orthorhombic values are shown in Table 1.1 only for comparison [4].

Theoretical electronic band structures were also calculated by various groups. Because these calculations were heavily dependent on crystal structure data, the bandgap predictions varied widely across the different studies. An example of the calculated band structures for $ZnSiN_2$, $ZnGeN_2$, and $ZnSnN_2$ are shown in Figure 1.3. The plots depicted show that all materials have direct band transitions, although some calculations determined that the lowest energy transition in $ZnSiN_2$ is indirect [5, 6]. Calculated bandgap values are listed in Table 1.2. The range of reported bandgap values spans a large portion of the visible and solar spectra, making this material system attractive for solid state lighting and solar

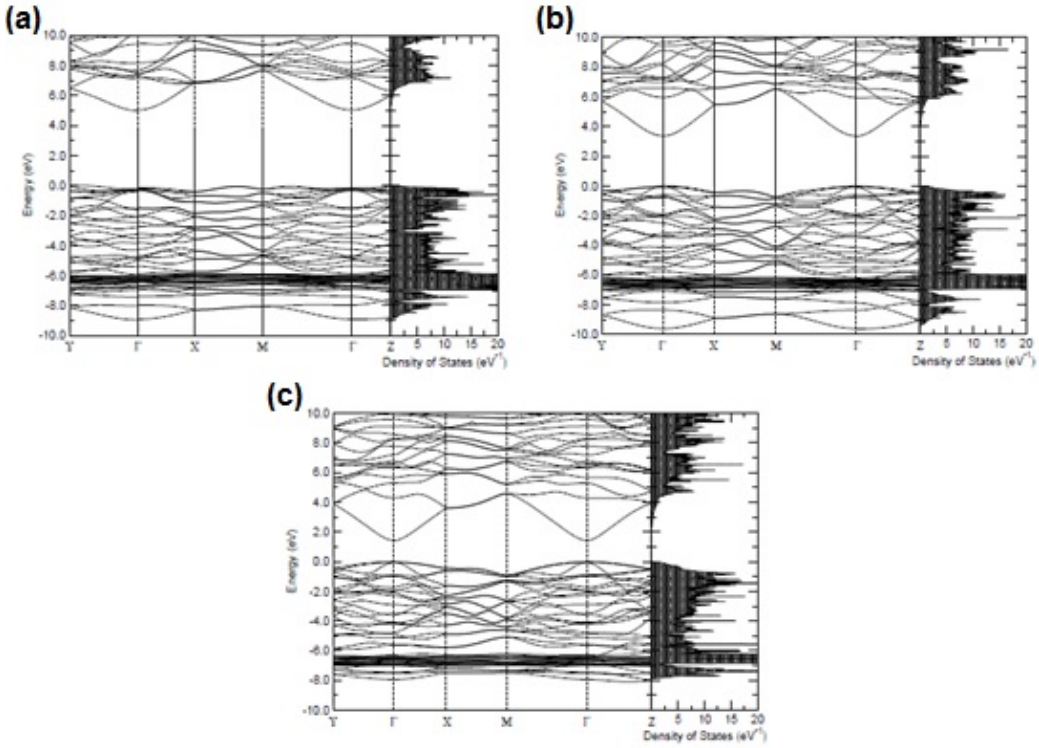

Figure 1.3. Calculated electronic band structures and density of states for (a) $ZnSiN_2$, (b) $ZnGeN_2$, and (c) $ZnSnN_2$. Data presented here indicates all materials have a direct bandgap. [1]

energy conversion applications. For comparison with the III-nitrides, a plot of theoretical bandgap vs. lattice parameter is shown in Figure 1.4. The accessible bandgap range is somewhat smaller in zinc-IV-nitrides, but the difference in lattice parameters is also smaller, suggesting that alloying and formation of heterostructures will be more straightforward.

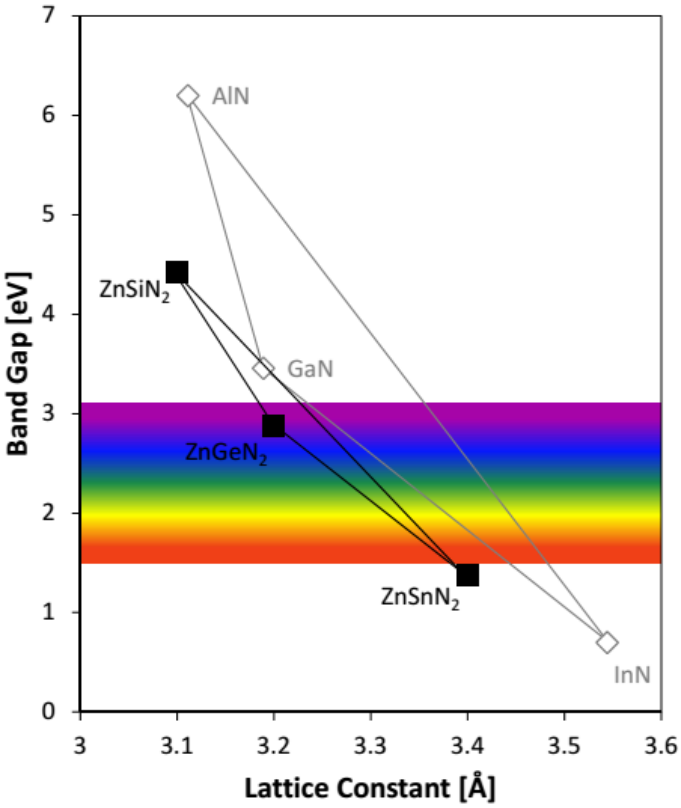

Figure 1.4. Theoretical bandgap vs. lattice constant of zinc-IV-nitrides. Known data points for the III-nitrides are included for comparison. The range of lattice constants and bandgaps is smaller for zinc-IV-nitrides. [1]

1.2.2 Synthesis

There are many examples in the literature of both $ZnSiN_2$ and $ZnGeN_2$ synthesis. $ZnSiN_2$ powder was synthesized using high-pressure annealing [2], and thin films have been grown on sapphire, (100) silicon, or silicon carbide by metalorganic chemical vapor deposition (MOCVD) [9-12]. More extensive efforts have been put into $ZnGeN_2$ fabrication, leading to powders made by reaction in a furnace [13-15], single crystal rods grown using a vapor-liquid-solid (VLS) method [16], and thin films deposited on glass and silicon by radio frequency (RF) sputter deposition and on sapphire and silicon carbide using MOCVD [9, 17-19]. Alloys of $ZnSiN_2$ and $ZnGeN_2$ have also been deposited by MOCVD [9, 12].

On the other hand, only very recently have reports surfaced of $ZnSnN_2$ synthesis. Polycrystalline crusts of $ZnSnN_2$ have been formed by a VLS method [20] and thin films were deposited by molecular beam epitaxy (MBE) [21].

1.2.3 Characterization

As with any new material, the first studies of zinc-IV-nitrides focused on characterizing the crystal structure. Drawing from theoretical predictions, the unit cell was expected to be a wurtzite-derived orthorhombic structure. However, various reports disagree about the exact symmetry of these materials. A compilation of experimental lattice parameter measurements are listed in Table 1.3 for the different crystal systems claimed. It should be noted that the difference between the different results is very small, as the monoclinic and orthorhombic crystals are simply slight distortions of the higher symmetry hexagonal

Table 1.3. Experimental lattice parameter measurements for zinc-IV-nitrides. *a*, *b*, and *c* values are in angstroms, and α, β, and γ values are in degrees.

	Crystal Structure	*a*	*b*	*c*	α	β	γ
$ZnSiN_2$	Orthorhombic [2]	5.2578(2)	6.3030(3)	5.0287(2)			
	Monoclinic [9]	3.09					
	Orthorhombic [10]	5.34	6.17	5.04			
	Orthorhombic [11]	5.05	6.18	5.35			
$ZnGeN_2$	Monoclinic [13]	3.157(024)	3.157(024)	5.137(021)			119.5
	Hexagonal [14]	3.193		5.187			
	Orthorhombic [22]	5.454	6.441	5.124			
	Hexagonal [17]	3.213		5.191			
	Orthorhombic [18]	5.50(20)	6.44(24)	5.14(25)			
	Hexagonal [19]	3.186(7)		5.174(12)			
	Monoclinic [23]	3.167	5.194	3.167			118.88
$ZnSnN_2$	Orthorhombic [20]	5.842(7)	6.753(6)	5.462(3)			
	Monoclinic [24]	3.395	3.4	5.534	89.885	90.033	120.036
	Monoclinic [4]	3.375(1)	3.376(1)	5.532(3)	89.98	89.99	119.93
	Monoclinic [4]	3.383(4)	3.379(3)	5.567(6)	89.97	89.96	119.95

one. Another important property was measurement of the electronic bandgaps of the different compounds. Experimental estimations of the bandgaps using absorption and photoluminescence are listed in Table 1.4. According to this data, the range of measured $ZnGeN_2$ bandgaps is quite large and there is no consensus on the value of the fundamental bandgap energy.

Additionally, there are a few reports on investigation of the electronic properties of zinc-IV-nitrides. One sample of $ZnGeN_2$ was found to be electrically insulating [17], while another was fairly conductive with a resistivity of 0.3-0.4 Ω·cm [14]. The discrepancy is

probably due to the difference in synthesis methods for each result. For the conductive material, electron concentrations and mobilities were also reported from Hall effect measurements of 10^{18}-10^{19} cm^{-3} and 0.5-5 $cm^2 \cdot V^{-1} \cdot s^{-1}$ [14]. Similar measurements of $ZnSnN_2$ films yielded electron concentrations of 10^{20}-10^{21} cm^{-3} and mobilities of 10 $cm^2 \cdot V^{-1} \cdot s^{-1}$ [4]. Studies of phonon modes in $ZnSiN_2$ and $ZnGeN_2$ have also been conducted using Raman and IR reflection spectroscopies [11, 15, 16, 25].

Table 1.4. Experimental electronic bandgap measurements for zinc-IV-nitrides. Values are reported in electron volts and represent direct transitions unless otherwise noted.

Reference	$ZnSiN_2$	$ZnGeN_2$	$ZnSnN_2$
[2]	3.64 (indirect)		
[9]	4.46	3.2	
[13]		3.40(1)	
[14]		2.67	
[15]		3.25	
[17]		3.1	
[26]		3.3	
[27]		2.99(2)	
[20]			1.7(1)
[4]			2.12, 2.38

1.3 Scope of Thesis

Based on the literature review of zinc-IV-nitride materials, there is certainly room for additional characterization, as the intrinsic properties of the materials are not well understood. For applications in optoelectronic devices, more information about the absorption and electronic properties of $ZnSnN_2$ and $ZnGeN_2$ would also be valuable, since these materials have bandgaps that are useful for interacting with visible light. A majority of the prior research has focused on studying $ZnGeN_2$ for use in optoelectronic devices because of the popularity of its III-nitride analogue, GaN. In this thesis, an emphasis will instead be placed on $ZnSnN_2$ as it is the least studied material with the most promise for visible light applications. Chapter 2 will describe the synthesis of $ZnSnN_2$ by reactive sputtering, for which synthesis had not yet been reported. Chapter 3 will explore tunable bandgap alloys by incorporating germanium to form $ZnSn_xGe_{1-x}N_2$. Optical bandgap characterization of various compositions will also be included here. Chapter 4 will discuss the challenges associated with carrier transport measurements, and tie the electronic properties of the materials back to the optical properties. Finally, Chapter 5 will summarize this thesis and identify topics for future work.

Chapter 2

Synthesis of Stoichiometric $ZnSnN_2$

At the outset of this project there was no evidence in the literature proving synthesis of $ZnSnN_2$, let alone any experimental characterization of its properties. Because of its predicted bandgap energy of 1.4 to 2 eV [3-5], this material is crucial for implementing the zinc-IV-nitride system of materials into optoelectronic devices that interact with visible light. It was therefore essential that the synthesis of $ZnSnN_2$ be made a priority to begin evaluating the potential of this material system as a whole.

This chapter describes the steps taken towards producing stoichiometric $ZnSnN_2$ by reactive radio frequency (RF) magnetron sputter deposition, a physical vapor deposition technique. Pulsed laser deposition (PLD) was another method used for initial synthesis attempts, but the conditions did not allow for the formation of a homogeneous material (see Appendix). The characterization of the structural properties of the sputter deposited material is also described here, as it was important for demonstrating that the desired material was created. Synthesis of single phase material was confirmed by studies of composition using energy dispersive X-ray spectroscopy (EDXS), and X-ray diffraction (XRD) revealed the wurtzite-derived $Pna2_1$ orthorhombic space group with unit cell parameters measured by selected area electron diffraction (SAED). Because of the lack of experimental research in the literature, verification of $ZnSnN_2$ synthesis chiefly relied on

comparison with theoretical predictions of space group and lattice parameters, as well as agreement with the patterns set by experimental work on $ZnGeN_2$ and $ZnSiN_2$. In addition, films were generally oriented with the *c*-axis perpendicular to the surface of the substrate, and were nearly epitaxial when grown on GaN, highlighting the smaller lattice mismatch compared to sapphire.

2.1 Sputtering Chamber Capabilities

The main advantage of using sputtering to synthesize $ZnSnN_2$ is that a reactive nitrogen source can be produced simply by allowing inert nitrogen gas into the chamber, where interaction with the sputtering plasma causes dissociation of the N_2 molecules. A schematic of a typical sputtering chamber is depicted in Figure 2.1. The sputtering process involves accelerating energetic ions towards a target material to eject atoms that then travel to the substrate, as well as the chamber walls. Ions are created by striking a plasma in an inert gas such as argon. These positively charged argon ions (Ar^+) are then accelerated towards the target by turning the target material into a negatively charged electrode (cathode). For magnetron sputtering, strong magnets are placed underneath the target in a specific pattern to create a trap for free electrons directly above the target surface, increasing the probability of ionizing neutral argon atoms. Because of the shape of the magnetic field, magnetron sputtering is marked by a circular “racetrack” pattern of erosion on the target. In RF sputtering, the target alternates between acting as a cathode and an anode. The purpose of this is to avoid charge buildup on the target surface, which can occur when DC generators are used on insulating target materials. Even though in this case the targets are metallic and should be able to dissipate any charge buildup, the addition of a reactive gas can potentially

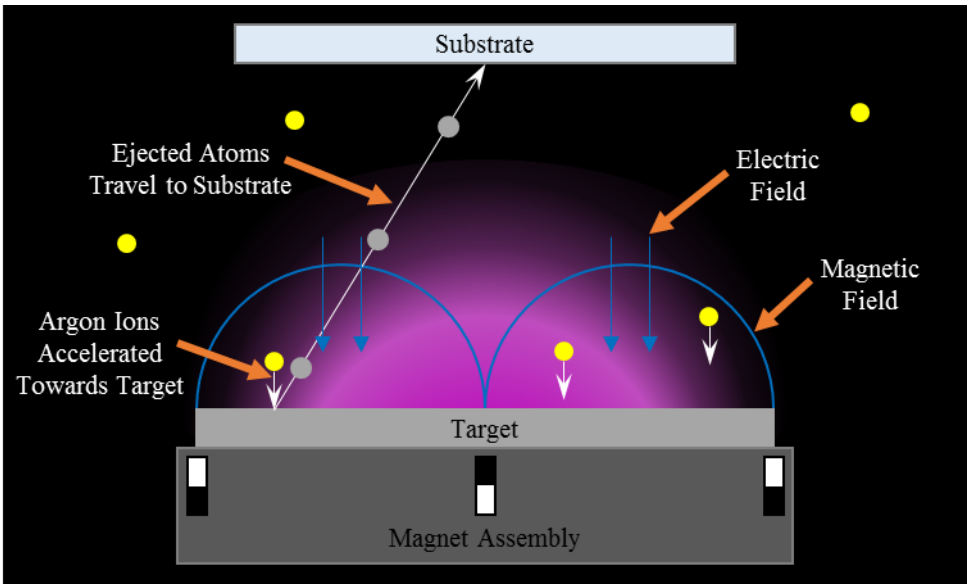

Figure 2.1. Schematic of reactive RF magnetron sputter deposition. A plasma generates energetic ions (Ar^+) that are accelerated towards a target, ejecting atoms that then travel to the substrate.

alter the composition of the target surface such that it becomes insulating. Reactive gas (typically nitrogen or oxygen) is often introduced in combination with the inert gas because the low atomic weight of the reactive gas alone makes it difficult to efficiently sputter metal targets. Changing the composition of the gas atmosphere in the chamber can also have an effect on the composition and morphology of the deposited film. These processes were all combined in the use of reactive RF magnetron sputtering to synthesize $ZnSnN_2$.

The deposition system used for these studies is an AJA International, Inc. ORION 8 UHV sputtering chamber equipped with seven magnetron sputtering sources, each accommodating target materials that are 2″ in diameter and 0.25″ thick. Each gun is powered by one of three RF generators or two DC generators controlled by a computer interface. The plasma is generally formed in an atmosphere of argon gas, and this system also has nitrogen and oxygen plumbed in for reactive sputtering. The substrate heater can

reach up to 850 °C, and the base pressure in the chamber is on the order of 10^{-7} Torr, but can be as low as 10^{-8} Torr after high-temperature baking.

2.2 Achieving Stoichiometric Films

In the initial exploration of $ZnSnN_2$ sputter deposition, it was first important to ensure that the desired stoichiometry could be achieved. Two different methods of deposition were studied: sputtering from a single mixed Zn_xSn_{1-x} target and simultaneously sputtering from elemental zinc and tin targets. The procedures for determining the optimal sputtering conditions for each method are discussed here. Tunable deposition parameters included substrate temperature, plasma power, gas pressure, and gas ratio. Film composition was measured using EDXS with an Oxford X-Max SDD system attached to a ZEISS 1550 VP field emission scanning electron microscope (SEM). The accelerating voltage in the SEM was kept at 7-10 kV to constrain the excitation volume to the thickness of the film, which is approximately 200-400 nm.

2.2.1 Sputtering From a Single Mixed Target

Early studies were carried out using a $Zn_{0.50}Sn_{0.50}$ pressed powder target acquired from ACI Alloys, Inc. with 99.99% purity. This target only allowed for stoichiometric film growth when the substrate temperature was below about 150 °C. At these low temperatures, the surface mobility of the adsorbed atoms is low and the crystalline quality of the film suffers. However at higher temperatures where the crystalline quality can be improved, the high vapor pressure of zinc leads to a low sticking coefficient and results in zinc-poor films. The

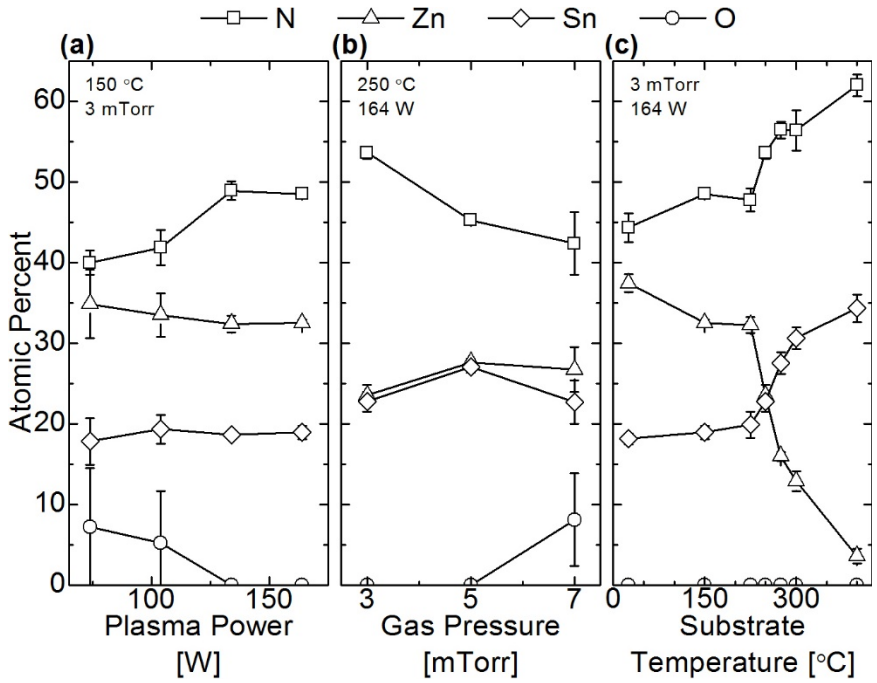

Figure 2.2. Optimization of deposition parameters when sputtering from a single $Zn_{0.75}Sn_{0.25}$ target. Composition measured by energy dispersive X-ray spectroscopy from films with varying (a) plasma power, (b) gas pressure, and (c) substrate temperature. Oxygen contamination is reduced in the films when plasma power is high and gas pressure is low. Desired zinc/tin ratio is achieved when the substrate temperature is near 250 °C. All other deposition parameters were held constant as indicated in the top left corner of each panel.

zinc desorption at high temperatures can be compensated by a zinc-rich source material, which prompted the use of a $Zn_{0.75}Sn_{0.25}$ pressed powder target for the remainder of the single target studies.

In optimizing the deposition conditions using the $Zn_{0.75}Sn_{0.25}$ target (99.99%, ACI Alloys, Inc.), it became evident that the first issue needing attention was excess oxygen incorporation in the films during growth. It was important to limit the oxygen to avoid characterization of zinc and tin oxides instead of the desired stoichiometric $ZnSnN_2$. Figure 2.2a-b shows the composition of the films as a function of the plasma power and gas

pressure. A significant amount of oxygen is found in films deposited at low plasma powers and high gas pressures. Both of these conditions decrease the deposition rate, which could be as low as 1 nm · min^{-1} for low powers and only a few nm · h^{-1} for high pressures. In these instances, the partial pressure of the deposited species is likely on the same order of magnitude as the partial pressure of oxygen in the chamber and both are deposited with comparable rates. Consequently, the combination of high plasma power and low gas pressure gives the lowest oxygen concentration in the resulting films, most likely correlating with an increased deposition rate and decreased relative partial pressure of oxygen. Figure 2.2a-b also shows that when varying the plasma power and gas pressure, there is no significant change in the ratio of zinc to tin, suggesting that the sputtering efficiency of zinc and tin remains proportional under the tested conditions. Additionally, the nitrogen composition appears to be inversely related to the amount of oxygen present in the films such that the oxygen is likely being substituted onto nitrogen sites in the lattice rather than being incorporated interstitially.

To control the zinc/tin ratio, the deposition temperature was varied using 164 W plasma power and a gas pressure of 3 mTorr, which is the best power/pressure combination identified to form a stable plasma and reduce the oxygen as much as possible. As illustrated in Figure 2.2c, the films are highly zinc-rich below 200 °C, at which point a drastic drop in zinc concentration occurs that correlates with the increase in tin and nitrogen atomic percentages. However, the growth window for avoiding excessive zinc desorption is rather small, as above 300 °C the layers become tin-rich. Therefore, the layer stoichiometry is strongly sensitive to the temperature when sputtering from a single mixed target, allowing for a small growth window of about 250 ± 25 °C. Under these conditions, material with the

desired stoichiometry for $ZnSnN_2$ could be deposited reliably, but there is little room for variation of the film properties.

2.2.2 Sputtering From Two Elemental Targets

Co-sputtering is a more desirable growth method because it has the advantage of being able to more accurately control the atomic fluxes for each individual metal. In the case of $ZnSnN_2$, the single mixed targets also limited the temperature range for stoichiometric growth. Removing the restriction of a fixed metal ratio could expand this temperature range, which would be useful for altering the film morphology. Another benefit of co-sputtering that was discovered during these investigations is that the rate of

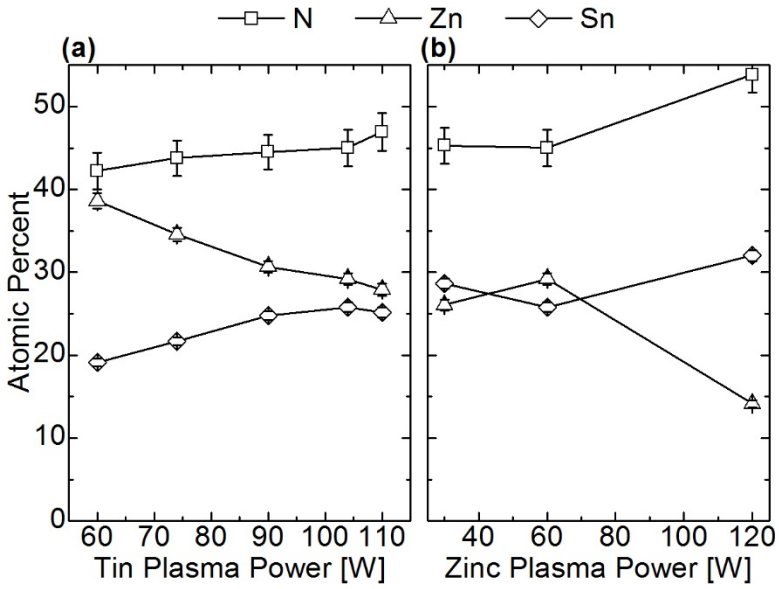

Figure 2.3. Optimization of deposition parameters when co-sputtering from elemental targets. Composition measured by energy dispersive X-ray spectroscopy from films with (a) 60 W zinc plasma power and varying tin plasma power and (b) zinc/tin plasma power ratio of 0.58 and varying the magnitude of the plasma powers. The plasma power ratio for stoichiometric deposition changes as the magnitude of the powers is changed.

sputtering is higher for elemental targets than for mixed targets. The reason for this is unclear, but may be due to changes in bond energy from alloying of zinc and tin or differences in the structure of the targets. The mixed targets are likely porous since they are made from a pressed powder, while the elemental targets are machined from a solid piece of cast metal. An advantageous effect of having a larger sputter yield is that one could expect decreased oxygen incorporation in the film, based on the results from single target sputtering experiments. This allows for the use of lower plasma powers and higher gas pressures, both of which tend to encourage growth of higher quality material. Conversely, adding another variable to the deposition process unfavorably adds to the complexity of the optimization procedure. The elemental zinc and tin targets were acquired from the Kurt J. Lesker Company with 99.99% and 99.999% purity, respectively. In light of the increase in adjustable deposition parameters, the extent of the range of growth options was explored initially. The focus was mainly held on varying the substrate temperature and plasma powers, but alterations in the gas pressure and gas composition were also studied.

First, an appropriate ratio of zinc and tin plasma powers was required that would result in stoichiometric material. Figure 2.3a shows how the composition changes with tin plasma power while the zinc plasma power is held constant at 60 W. All samples were grown at 170 °C in 3 mTorr of a 75% N_2 atmosphere, and the tin power was increased until the desired stoichiometry was achieved. For this particular set of samples, the zinc/tin ratio is not exactly 1:1, so the tin power could have been increased even more. Once a ratio of plasma powers was selected for a given substrate temperature, the effect of the magnitude of the power was tested. Composition measurements for samples deposited with a constant zinc/tin plasma power ratio of about 0.58 are shown in Figure 2.3b as a function of the zinc

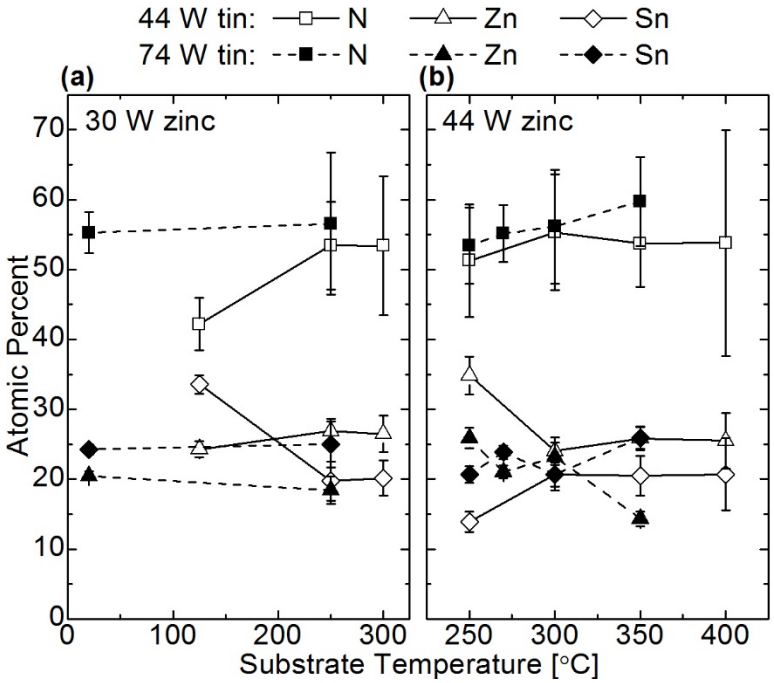

Figure 2.4. Optimization of deposition parameters when co-sputtering from elemental targets. Composition measured by energy dispersive X-ray spectroscopy from films with (a) 30 W zinc and (b) 44 W zinc as a function of substrate temperature. Open symbols with solid lines indicate a tin plasma power of 44 W, and closed symbols with dashed lines indicate a tin plasma power of 74 W. Films are close to stoichiometric over a large range of substrate temperatures.

plasma power. With larger plasma powers, the composition is far from stoichiometric even though the ratio of the zinc and tin powers was the same as the other data points. Sputter yields are generally not expected to be linear, making this an unsurprising result, but it does highlight the expanse and complexity of the deposition phase space being explored here.

The next variable tested was the substrate temperature because this parameter was notably restricted in the optimization of single mixed target deposition and could be interesting for altering the film morphology. Samples were deposited with the same zinc/tin plasma power ratio of about 0.58 in 3 mTorr of a 75% nitrogen atmosphere over a range

of substrate temperatures. The plasma powers included 30 W and 44 W for zinc and 44 W and 74 W for tin. The compositions if these samples are displayed in Figure 2.4a-b as a function of substrate temperature. Surprisingly, the overall results do not appear to change as dramatically as in the single target temperature study. One would expect the zinc content to decrease at higher temperatures due to its high vapor pressure, but near-stoichiometric films were deposited up to about 400 °C. Only for the samples deposited with a tin plasma power of 44 W is the composition significantly far from stoichiometry. This condition occurs at 125 °C for a zinc power of 30 W (Figure 2.4a) and at 250 °C for a zinc power of 44 W (Figure 2.4b). These data points could simply be outliers, so additional replicates of the conditions shown are needed to confirm the results. What this data does show is that it is possible to synthesize near-stoichiometric films over a very wide range of temperatures.

Like the results from the single target studies, changes in the gas pressure did not have a significant effect on the metal composition in the films (Figure 2.5a). Oxygen incorporation still increased with increasing pressure and decreased with an increasing plasma power.

The last parameter tested was the amount of nitrogen present in the atmosphere during deposition. Figure 2.5b shows the composition of films as a function of the percent nitrogen in the argon/nitrogen gas mixture. All samples used 44 W of zinc power, 74 W of tin power, 3mTorr gas pressure, and a substrate temperature of 250 °C. The most obvious result is that the nitrogen content in the film is low when the percent nitrogen in the atmosphere is also low. This can be observed in the sample deposited with 25% nitrogen gas. However, nitrogen is not the only element whose incorporation is affected by a change in the gas composition. The ratio of zinc to tin measured in the films is lower for samples

deposited with 25% and 50 % nitrogen compared to the ones deposited with 75% and 100% nitrogen. This is probably due to the changing mass of the gas mixture and the difference in sputtering efficiency between the two metals. Because tin is a heavier element compared to zinc, it is more efficiently sputtered by the heavier argon ions. When the gas ratio favors argon, more tin will be sputtered and deposited on the substrate, decreasing the zinc/tin ratio in the film. Finally, even though the film composition for samples deposited in 75% and 100% nitrogen are similar, use of 75% nitrogen was preferred because of the higher deposition rate.

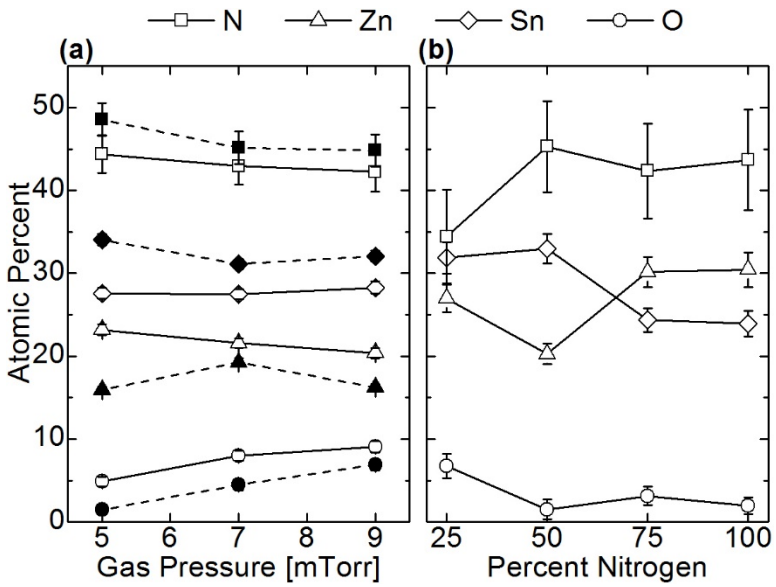

Figure 2.5. Optimization of deposition parameters when co-sputtering from elemental targets. Composition measured by energy dispersive X-ray spectroscopy from films with (a) varying gas pressure and zinc/tin plasma powers of 60/110 W (open symbols) and 120/210 W (closed symbols) and (b) varying nitrogen content in the chamber atmosphere. Gas pressure only appears to affect oxygen incorporation, and is decreased at higher plasma powers. Low nitrogen gas content results in decreased nitrogen in the film and increased sputtering of tin.

2.3 Characterization of the Crystal Structure

Composition measurements alone could not ensure that the deposited films consisted of a phase-pure compound semiconductor material. For example, the material could have been made up of domains of zinc, tin, or the nitrides or oxides of those elements. To prove that the deposited material is in fact the correct phase of $ZnSnN_2$, the crystal structure of the films was characterized in addition to measuring the stoichiometric composition. Powder XRD measurements indicated that the material is crystalline with a wurtzite-derived unit cell, confirming the theoretical calculations for $ZnSnN_2$ [3, 5, 7]. Additionally, the lattice parameters within the unit cell, which are important for material identification, were measured by XRD and SAED of the deposited films.

2.3.1 Space Group

Powder diffraction patterns were measured from a ground up thick film that was removed from the substrate to determine the phase of the sputtered material. The position and relative intensity of peaks in a powder diffractogram are a type of "fingerprint" allowing identification of distinct materials, where each peak represents a spacing between atomic planes within the unit cell of the crystal. The assumption made in this measurement is that the particles in the powder are sufficiently small and randomly oriented such that all interplanar spacings of the unit cell are represented. Measurements were made using a PANalytical X'Pert Pro powder diffractometer over a 2θ range of 20° to 80°. The X-rays are generated with a Cu Kα source, which creates photons with a wavelength of about 1.54 Å.

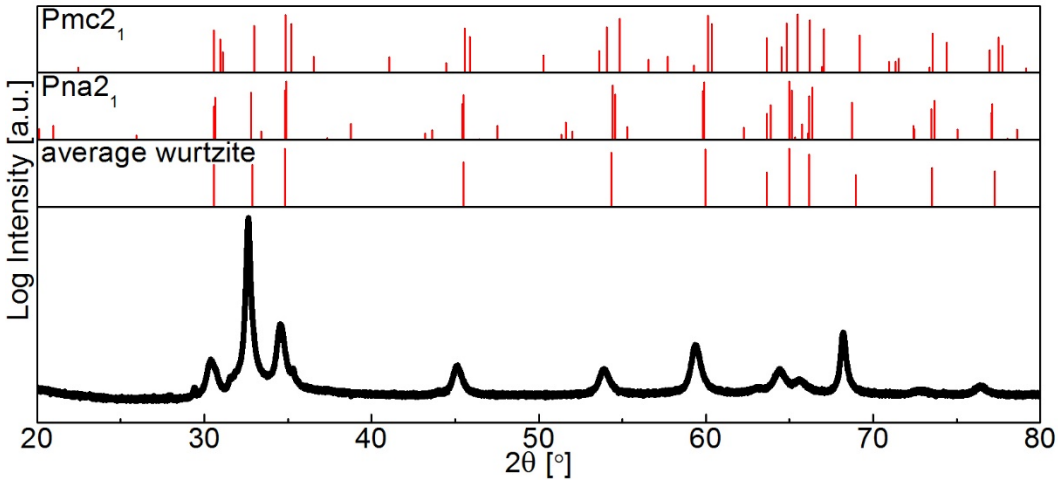

Figure 2.6. Powder diffraction spectrum of $ZnSnN_2$ measured by X-ray diffraction. Peak positions are also shown that were calculated from theoretical zero Kelvin lattice parameters for the $Pmc2_1$, $Pna2_1$, and average wurtzite structures. $Pmc2_1$ and $Pna2_1$ are both ordered orthorhombic unit cells, and the average wurtzite unit cell assumes random ordering of zinc and tin atoms.

To prepare powder samples for measurement, an alumina mortar and pestle was used to grind $ZnSnN_2$ films adhered to sapphire substrates. The films were on the order of 10^2 nm thick while the substrate thickness was 0.5 mm or 0.1 mm. For both substrate thicknesses, the strong diffraction from the single crystal sapphire obscured the measurement of peaks corresponding to the film. Making a film that is thicker than the substrate was not feasible, as it would require 400-500 h of deposition time to reach a suitable thickness. Instead, a film was deposited on a 2″ sapphire wafer to a thickness of a few μm and removed from the substrate by rapid thermal annealing (RTA). The sample was ramped up to 600 °C over 30 s and held at that temperature for 60 s before passively cooling back to room temperature. Because of the large difference in thermal expansion coefficient between $ZnSnN_2$ and sapphire, the film cracks and flakes off of the substrate

under the thermal stress. The flakes were then collected and ground into a fine powder using the mortar and pestle.

The measured powder diffractrogram is shown in Figure 2.6. Theoretical peak positions based on calculated zero Kelvin lattice parameters [3] for $Pna2_1$, $Pmc2_1$, and an average wurtzite structure, representing a random distribution of zinc and tin atoms, are shown for comparison. The measured pattern matches well with the $Pna2_1$ and average wurtzite structures, where the most apparent distinguishing feature is a slight splitting of some peaks in the $Pna2_1$ structure. Although it appears that the $ZnSnN_2$ diffraction pattern does not contain split peaks, it should be noted that the full width at half maximum (FWHM) of the peaks that would be split in the $Pna2_1$ case is large compared to the peaks that are not expected to be split. This suggests that the $Pna2_1$ space group describes the predominant arrangement of metallic atoms in the measured sample. This is consistent with reports on synthesis of $ZnGeN_2$ and $ZnSiN_2$ materials, where several groups have shown that they both exhibit the $Pna2_1$ structure [2, 15, 18, 22, 28]. Another important piece of evidence to point out is that the peaks present in the samples do not match with the diffraction patterns for Zn or Sn metals, nor with the patterns of the oxides or nitrides of those elements. This further supports the claim that the material being created and characterized is in fact $ZnSnN_2$.

2.3.2 Lattice Parameter Measurements

After determining that the space group is orthorhombic, the lattice parameters can be accurately measured by using different diffraction techniques. The powder diffraction data shown in Figure 2.6 was not suitable for making these measurements since there was no

internal standard included in the powder sample to calibrate the peak positions. Instead, XRD measurements of films on the substrate were made with the system aligned to the substrate peak. The disadvantage of using this method is that only the atomic planes that are parallel to the surface of the substrate can be observed. In addition, SAED patterns were measured in a transmission electron microscope (TEM) to gain information about interplanar distances in other directions.

The majority of the crystalline $ZnSnN_2$ films deposited on sapphire or GaN were oriented with the *c*-axis perpendicular to the plane of the substrate. This allowed for the measurement of the *c* lattice constant using θ-2θ XRD and Bragg's Law given in Equation (2.1), where d_{hkl} is the distance between (*hkl*) planes, *n* is a positive integer, λ is the wavelength of the incident X-rays, and θ_{hkl} is the angle between incoming X-rays and the surface of the crystal that results in diffraction from (*hkl*) planes:

$$d_{hkl} = \frac{n\lambda}{2 \sin \theta_{hkl}} \quad . \tag{2.1}$$

Since the (*hkl*) plane being observed in the $ZnSnN_2$ films is the (002) plane, the calculated interplanar spacing is equal to half of the *c* lattice constant. θ-2θ XRD measurements were made using a PANalytical X'Pert Pro MRD over a 2θ range of 25° to 45° and aligned to the sapphire (0006) peak. The average 2θ peak position of (002) planes for a number of films on sapphire was about 32.4°, corresponding to a *c* lattice constant of 5.52 ± 0.01 Å.

To measure the *a* and *b* lattice constants, SAED patterns were imaged on a CCD camera using an FEI Tecnai TF30 TEM operated at 300 kV. A double-tilt sample holder was used in the microscope to more easily align the electron beam to the zone axis of the substrate. Due to the use of electromagnetic lenses in the microscope, the camera length

does not represent a fixed physical length and requires calibration before analyzing the film. This was done by measuring known diffraction spots in the images. In this case, SAED patterns were taken of the substrate alone using the same camera length setting as for the film and the actual camera length, L, was calculated by

$$L = \frac{R_{hkl} d_{hkl}}{\lambda} \quad , \tag{2.2}$$

where R_{hkl} is the distance between the transmitted and (*hkl*) diffracted beams in the SAED image, d_{hkl} is the distance between (*hkl*) planes, and λ is the wavelength of the electrons (about 1.97 pm for 300 kV electrons). Known substrate lattice parameters used for the calculations were a = 4.759 Å and c = 12.992 Å for sapphire, and a = 3.189 Å and c = 5.185 Å for GaN. The camera length was calibrated to be 740 mm for the sample on sapphire and 392 mm for the sample on GaN. The difference between the two is only due to changes in the microscope settings.

To measure the lattice parameters, the diffraction spots in the SAED patterns of $ZnSnN_2$ films needed to be indexed. These indexed patterns are displayed in Figure 2.7a-b for $ZnSnN_2$ on both substrates. The procedure for indexing is similar to calibrating the camera length, only in reverse. Equation (2.2) can be rearranged so that L, λ, and R_{hkl} are used to calculate d_{hkl} for each diffraction spot. Calculated d_{hkl} spacings based on measured R_{hkl} values are listed in Figure 2.7a-b for both patterns. The interplanar distances were then compared to values derived from theoretically calculated lattice constants [3] to assign a Miller index, (*hkl*), to each diffraction spot. The theoretical d_{hkl} values corresponding to the measured spots are also included in Figure 2.7a-b for comparison. Lattice constants were then calculated from the d_{hkl} of planes perpendicular to the unit cell faces, i.e. (100), (010),

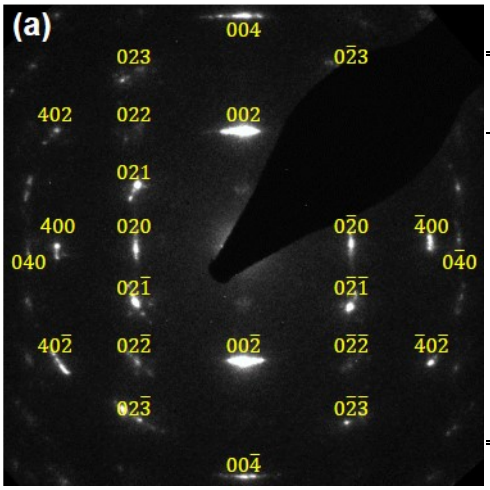

(*hkl*)	Experimental d_{hkl} [Å]	Theoretical d_{hkl} [Å]
(020)	2.928	2.921
(002)	2.735	2.730
(021)	2.585	2.575
(022)	1.986	1.994
(400)	1.692	1.680
(023)	1.547	1.544
(040)	1.465	1.461
(004)	1.375	1.365

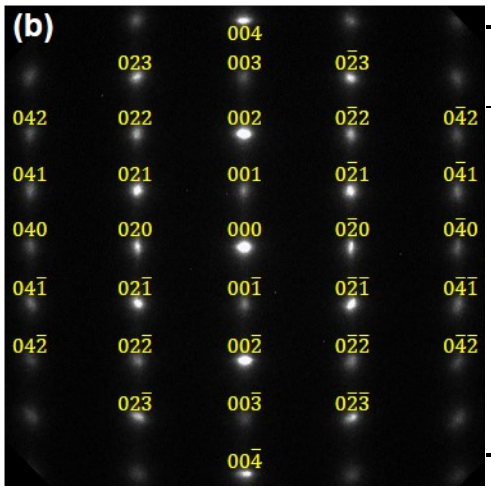

(*hkl*)	Experimental d_{hkl} [Å]	Theoretical d_{hkl} [Å]
(020)	2.883	2.921
(002)	2.750	2.730
(021)	2.558	2.575
(022)	1.998	1.994
(023)	1.563	1.544
(040)	1.450	1.461
(004)	1.386	1.365
(060)	0.965	0.974
(006)	0.930	0.910

Figure 2.7. Indexed selected area electron diffraction patterns for $ZnSnN_2$ films on (a) *c*-sapphire and (b) *c*-GaN substrates. Tables present experimental interplanar lattice spacings, d_{hkl}, calculated from measured distances between spots in the diffraction patterns. Miller indices, (*hkl*), were assigned by comparing experimental and theoretical interplanar distances [3].

and (001). On sapphire, the measured $ZnSnN_2$ lattice constants are a = 6.766 Å, b = 5.857 Å, and c = 5.485 Å. Measurement of both the a and b constants was only possible because the grains in the film on sapphire were oriented in multiple planar directions. On GaN, the a lattice constant was not measureable because the grains were mostly oriented in the same direction, with the (100) planes perpendicular to the electron beam. However, the other constants were measured to be b = 5.786 Å and c = 5.542 Å. Table 2.1 also presents theoretical lattice constants for comparison.

In the case of $ZnSnN_2$ on sapphire, the measured lattice constants agree fairly well with the theoretical zero Kelvin lattice constants [3], with each one differing by less than 1% from the theory. Some disagreement is expected because the measurements were made at room temperature, where thermal energy would cause an expansion of the zero Kelvin unit cell, and in fact the measured values are all larger than the theoretical constants. The film on GaN, however, deviates more from the theoretical values with differences of -1% and 1.5% for the b and c parameters, respectively. One possible explanation for this is that the $ZnSnN_2$ film was strained to the GaN lattice, while the sapphire lattice mismatch was so large that the $ZnSnN_2$ grew as a relaxed film. For comparison, if the hexagonal wurtzite lattice were described by a $Pna2_1$ unit cell instead, its "b" lattice constant would be equal to $a_h \cdot \sqrt{3}$, where a_h is the a constant in the hexagonal unit cell. These "b" values are 5.524 Å for GaN and 8.243 Å for sapphire. The fact that the measured b parameter is smaller than the predicted value for $ZnSnN_2$ on GaN supports the hypothesis that the film is strained, as the $ZnSnN_2$ unit cell would be required to compress in the b direction to align with the GaN lattice.

Table 2.1. Measured $ZnSnN_2$ lattice constants. Values were derived from measured (100), (010), and (001) interplanar distances. Theoretical lattice constants are also included for comparison. All numbers are reported in angstroms.

Lattice Parameter	Experimental (on sapphire)	Experimental (on GaN)	Theoretical
a	6.766		6.721 [3] 6.76 [7] 6.59, 6.70 [5]
b	5.857	5.786	5.842 [3] 5.85 [7] 5.70, 5.80 [5]
c	5.485	5.542	5.459 [3] 5.58 [7] 5.41, 5.53 [5]

2.4 Film Structure and Morphology

From the previously discussed composition and crystal structure measurements, it was reasonably clear that single phase $ZnSnN_2$ could be synthesized. The next task was to study the morphology of the films and see how the deposition conditions affected the structure. θ-2θ XRD measurements of films on their substrates were used for these studies, which only allow for observation of atomic planes that are parallel to the surface of the substrate. The majority of the deposited $ZnSnN_2$ films on *c*-sapphire and *c*-GaN substrates were oriented such that the (002) reflection peak was the only one visible. Observation of other orientations indicated a highly polycrystalline material without any relationship to the substrate.

A major issue was encountered when attempting to quantify the effect of varying deposition conditions on the structure of the films. For material grown on *c*-sapphire

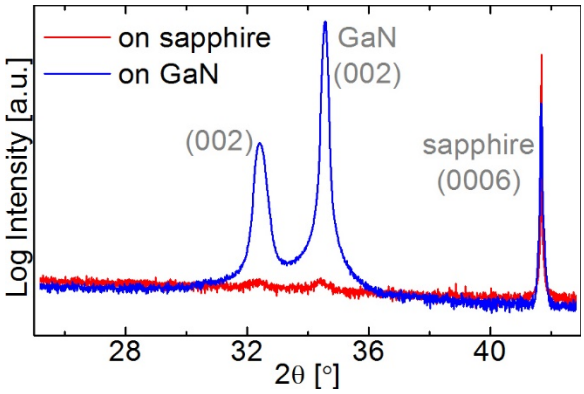

Figure 2.8. θ-2θ X-ray diffraction data from stoichiometric $ZnSnN_2$ films deposited at the same time on *c*-sapphire and *c*-GaN substrates, meaning deposition conditions were exactly the same. Crystalline film was able to grow on GaN, but an unknown factor hindered high quality growth on sapphire.

substrates, the (002) peak was not consistently observed in films deposited under the same conditions. It is still unclear what factors were ultimately hindering the reproducibility of the deposited film structure. One possible reason is related to the volatility of zinc. During these experiments, co-sputtered $ZnSnN_2$ films deposited consecutively under the same conditions were observed in XRD to have (002) peaks that decreased in intensity and eventually disappeared. Zinc also appeared to accumulate in the vacuum chamber, manifesting as an increase in zinc content for films deposited later in the series. It is therefore possible that excess zinc left in the chamber interferes with nucleation or deposition of subsequent material.

Whatever the origin for this lack of reproducibility, it turned out not to affect the crystallinity of films deposited on *c*-GaN substrates. This is probably a result of the smaller lattice mismatch between $ZnSnN_2$ and GaN, compared to that of $ZnSnN_2$ and sapphire, making it easier to form crystalline material when the conditions are not perfect. Figure 2.8 shows θ-2θ XRD measurements from stoichiometric $ZnSnN_2$ films deposited together on

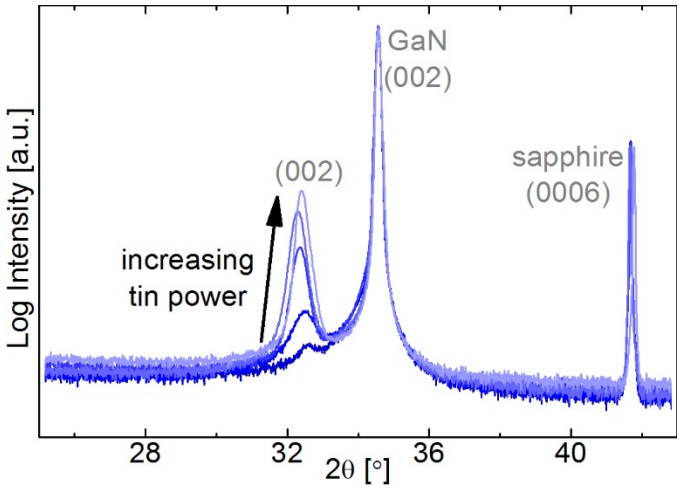

Figure 2.9. θ-2θ X-ray diffraction data from $ZnSnN_2$ films deposited with 60 W zinc plasma power and varying tin plasma power. (002) peak loses intensity and broadens as the tin power is decreased and film composition deviates further away from stoichiometry (Figure 2.3a).

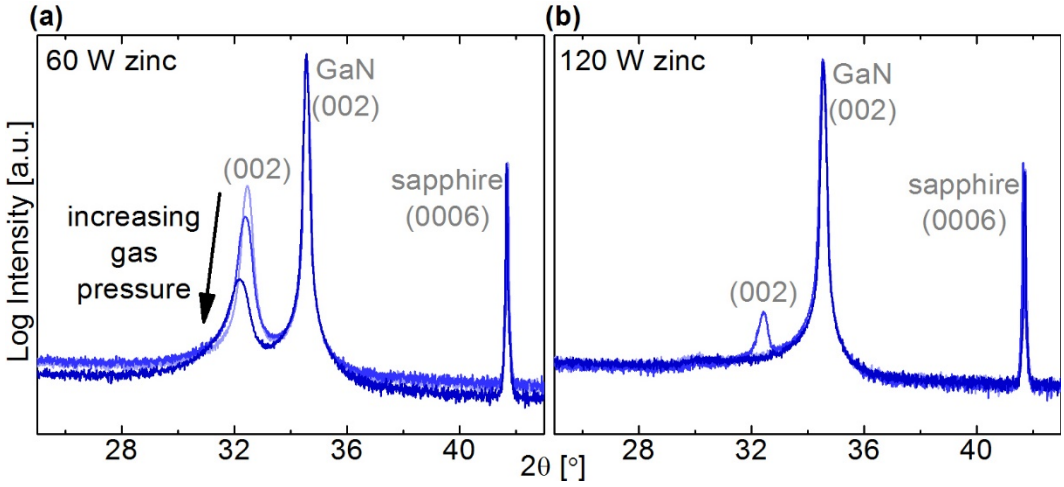

Figure 2.10. θ-2θ X-ray diffraction data from $ZnSnN_2$ films with varying gas pressure and zinc/tin plasma powers of (a) 60/110 W and (b) 120/210 W. (002) peak loses intensity and broadens as gas pressure is increased. Deposition using higher power results in mostly amorphous material.

c-sapphire and *c*-GaN, meaning all of the deposition conditions were exactly the same. The film on *c*-GaN is crystalline and textured with a very sharp (002) peak around 32.4°, while the film on *c*-sapphire is amorphous or possibly nanocrystalline. As a result, a few studies were carried out to examine the structural effect of varying deposition conditions using only *c*-GaN substrates. XRD measurements from the same samples examined in Figure 2.3a are shown in Figure 2.9. As the film composition moves further away from stoichiometry, the (002) peak loses intensity and broadens, indicating that the material structure is becoming increasingly disordered. Similarly, XRD from the samples examined in Figure 2.5a are shown in Figure 2.10a-b. For films deposited with 60 W zinc plasma power, the (002) peak loses intensity and broadens as the gas pressure is increased.

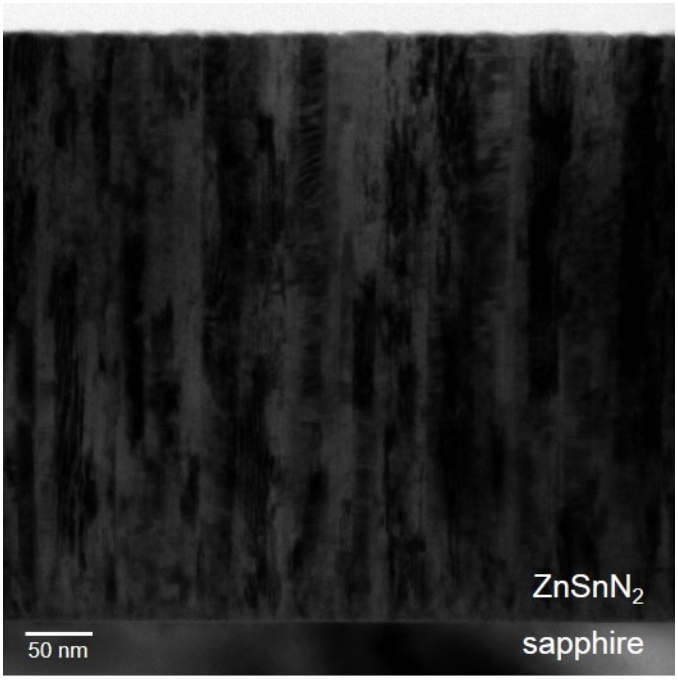

Figure 2.11. Transmission electron microscope bright field image of $ZnSnN_2$ on *c*-sapphire substrate viewed in cross-section. Grains are columnar and less than 50 nm wide, which is typical for sputtered material.

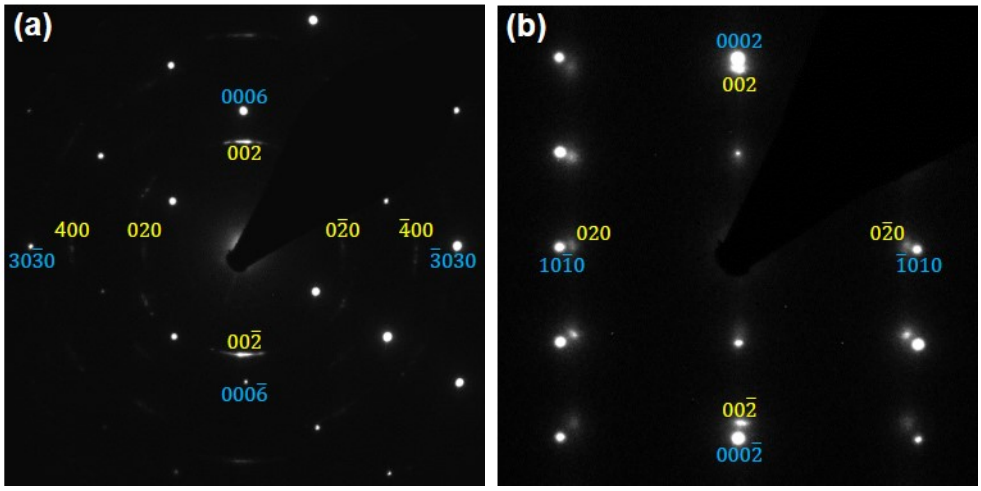

Figure 2.12. Selected area electron diffraction patterns from the interface of $ZnSnN_2$ films on (a) *c*-sapphire and (b) *c*-GaN substrates. Diffraction spots indicate that the *c*-plane in $ZnSnN_2$ is aligned to the *c*-plane of sapphire and of GaN. Additionally, (10$\underline{1}$0) substrate planes are aligned with (100) and (010) $ZnSnN_2$ planes on sapphire and only with (010) $ZnSnN_2$ planes on GaN. Miller indices in yellow belong to $ZnSnN_2$ and indices in blue belong to the substrate.

The resulting increase in oxygen incorporation in the films likely forms an abundance of defects in the crystal structure, which causes the change in the peak shape. When the power is increased to 120 W zinc plasma power, the XRD measurements reveal that the material is mostly amorphous, even though the oxygen content is lower in these films. The higher plasma power may cause the substrate and growing film to be bombarded by higher energy sputtered molecules that can disrupt the crystal structure.

Transmission electron microscopy was also used to study the morphology of the films. Figure 2.11 shows a TEM bright field image of a cross-sectional sample of $ZnSnN_2$ deposited on a *c*-sapphire substrate. The film clearly consists of columnar grains that are less than 50 nm wide. The grain size also appears to increase towards the surface of the film as grains coalesce during growth. SAED from the same film's interface (Figure 2.12a)

shows that the grains are aligned with the substrate such that either the (010) or (100) atomic planes are parallel with the (10$\underline{1}$0) plane in the sapphire. This indicates that some grains are rotated 90° from each other in the plane of the substrate. In contrast, the SAED from a film grown on a *c*-GaN substrate shows only one in-plane direction for the $ZnSnN_2$ grains (Figure 2.12b). These results again reinforce the conclusion that higher quality $ZnSnN_2$ is grown on GaN because of the smaller lattice match.

2.5 Conclusion

Presented in this chapter is the optimization of deposition parameters to achieve single phase $ZnSnN_2$, a new earth-abundant semiconductor. This compound is important for demonstrating the applicability of the entire zinc-IV-nitride material system in visible light optoelectronic devices. Furthermore, $ZnSnN_2$ was able to be synthesized using a cost-effective and scalable deposition method, strengthening its potential for large-scale device applications.

Stoichiometric single phase $ZnSnN_2$ was synthesized using reactive RF magnetron sputter deposition from a single mixed Zn_xSn_{1-x} target or from elemental zinc and tin targets. Co-sputtering provides for an expansive array of variable deposition parameters, of which only a small portion has been explored here. EDXS composition measurements were used to optimize the deposition conditions for reducing oxygen contamination and achieving a zinc/tin ratio of close to 1 in the deposited film. The material exhibited the predicted $Pna2_1$ wurtzite-derived orthorhombic crystal structure with lattice parameters measured from SAED patterns that agree with theoretical values. The morphology of the films was also studied using XRD and TEM. Grains are columnar and small, less than 50 nm, which is

typical of sputtered material. The choice of substrate also played a large role in making high quality material. The smaller lattice mismatch to GaN, compared to sapphire, allowed for growth of highly crystalline and textured $ZnSnN_2$ films that were strained at the interface to match with the lattice of the substrate.

In the next chapter, exploration of the zinc-IV-nitride material system will be extended by alloying $ZnSnN_2$ with $ZnGeN_2$, resulting in an earth-abundant tunable bandgap semiconductor that spans a majority of the visible spectrum. Optical properties of these alloys will be characterized to determine if they can potentially serve as an alternative to $In_xGa_{1-x}N$ in optoelectronic devices.

Chapter 3

Tunable Bandgap $ZnSn_xGe_{1-x}N_2$ Alloys

In recent years, $In_xGa_{1-x}N$ alloys have attracted attention in the scientific community because of their demonstrated success in optoelectronic devices, especially those that interact with visible light such as light-emitting diodes (LEDs) and photovoltaics. For such applications, $In_xGa_{1-x}N$ is ideal because the direct bandgap is tunable over a theoretical range of 0.7 eV to 3.4 eV by changing the amount of indium in the alloy, and high quality material can be grown with large absorption coefficients and mobilities. However, $In_xGa_{1-x}N$ alloys with high indium content have been difficult to grow because InN and GaN have a large difference in lattice parameters, leading to indium segregation and phase separation. Extensive research has been conducted in pursuit of overcoming this problem so that the entire theoretical bandgap range can be accessed. Incorporating more than about 30% indium into the alloy results in phase separation, which limits the bandgap to the blue range of the visible spectrum. This is generally referred to as the “green gap” in the LED industry, as researchers have been unable to produce an efficient green LED that emits between 520 and 530 nm. Even though there are more sophisticated growth strategies for $In_xGa_{1-x}N$ that allow for near-green emission, such as quantum well structures, the scarcity and cost of indium will limit its large-scale deployment.

Based on theoretical predictions, earth-abundant $ZnSn_xGe_{1-x}N_2$ is expected to have similar optical and electronic properties to $In_xGa_{1-x}N$ [7], and can potentially be tuned to span an energy range of 1.4 eV to 2.9 eV, which still covers the majority of the visible spectrum. Although the alloy has a shorter range of predicted bandgaps, it also has a smaller lattice mismatch between its constituent materials, $ZnSnN_2$ and $ZnGeN_2$. This is a potential advantage for alloying because the large lattice mismatch is a major factor contributing to the phase separation of InN and GaN. If phase separation does not occur, $ZnSn_xGe_{1-x}N_2$ could be capable of closing the "green gap." Additionally, an efficient graded or multi-junction photovoltaic device could be developed with any combination of bandgaps between 1.4 eV to 2.9 eV. One simply needs to search the literature for $In_xGa_{1-x}N$ to have an idea of the range of optoelectronic devices that could benefit from an earth-abundant alternative.

In this chapter, $ZnSn_xGe_{1-x}N_2$ is synthesized by adding germanium to the sputtering process described in Chapter 2. A wide range of compositions with the correct zinc and nitrogen stoichiometry can be accessed using this method. X-ray diffraction (XRD) measurements show a linearly shifting (002) peak, indicating no phase separation. Spectroscopic ellipsometry reveals optical bandgaps that increase with increasing germanium incorporation from about 1.8 to 3.1 eV.

3.1 Linear Incorporation of Germanium to Form $ZnSn_xGe_{1-x}N_2$

$ZnSn_xGe_{1-x}N_2$ thin films were deposited on *c*-sapphire and *c*-GaN substrates by reactive radio frequency (RF) co-sputtering from metal targets in an argon/nitrogen plasma. The

gas pressure was held at 3 mTorr during deposition with 75% nitrogen in the plasma. To encourage crystalline growth, the substrate temperature was set to about 270 °C. For $ZnSn_xGe_{1-x}N_2$ with x = 0 or 1, films were deposited by co-sputtering from zinc (99.99%) and germanium (99.999%) or zinc and tin (99.999%) elemental targets, all obtained from the Kurt J. Lesker Company. An RF power of 44 W was applied to the zinc target, while the tin and germanium targets required 74 W and 104 W, respectively, to obtain stoichiometric films as determined by energy dispersive X-ray spectroscopy (EDXS). Films with $0 < x < 1$ were sputtered from a $Zn_{0.75}Sn_{0.25}$ pressed powder target (99.99%, ACI Alloys, Inc.) and a germanium elemental target because the sputtering system was limited to two RF power supplies at the time of these experiments. The combined target is zinc-rich because the high vapor pressure of zinc limits its incorporation during deposition at substrate temperatures above about 200 °C (see Chapter 2). For the data presented here, the RF power on the $Zn_{0.75}Sn_{0.25}$ target was kept at 134 W and the power applied to the germanium target was varied from 30 W to 134 W to create a set of samples with ranging compositions. As shown in Chapter 2, the combined target requires a higher power than the elemental targets to get a comparable deposition rate that limits oxygen incorporation in the film.

3.1.1 Measurements of Composition Variation

Figure 3.1 presents the composition measurements for $ZnSn_xGe_{1-x}N_2$ films on *c*-sapphire and *c*-GaN substrates using EDXS. An accelerating voltage of less than 10 kV was used to confine the size of the activation volume to the thickness of the thin films. All of the samples have close to 25 at% zinc and 50 at% nitrogen within error. The quaternary films

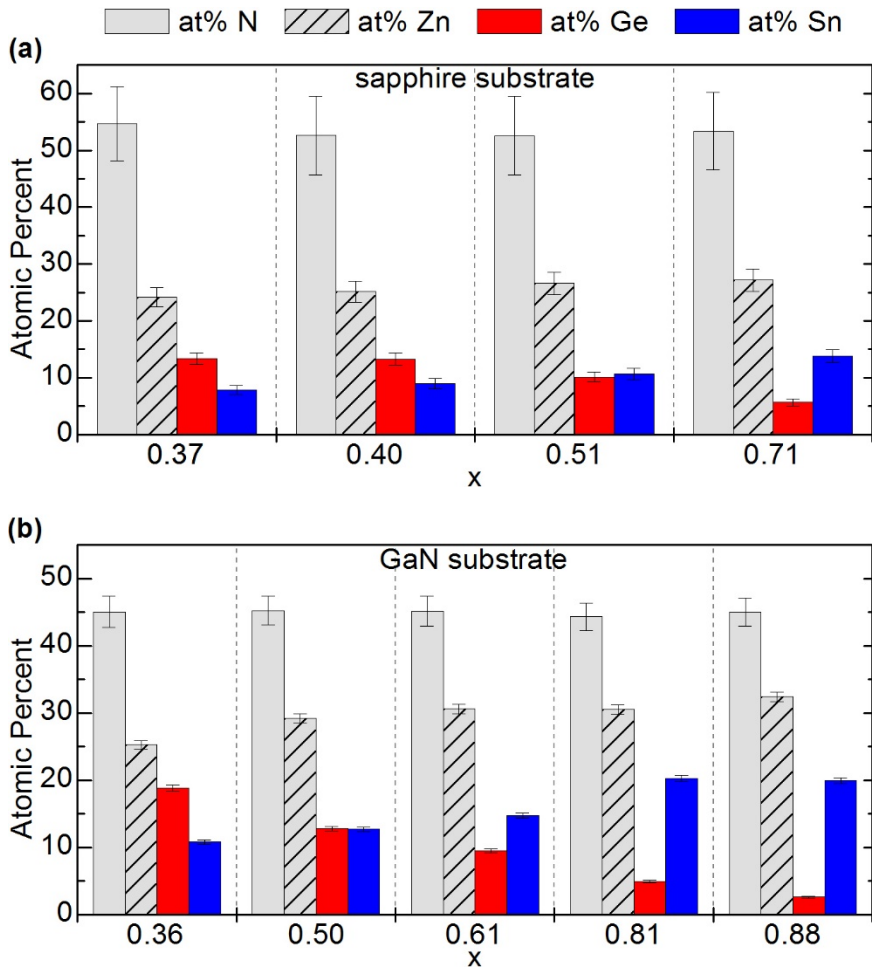

Figure 3.1. Composition of $ZnSn_xGe_{1-x}N_2$ films deposited on (a) *c*-sapphire and (b) *c*-GaN substrates measured by energy dispersive X-ray spectroscopy. Films on each substrate exhibit consistent zinc and nitrogen concentrations close to 25 at% and 50 at%, respectively. Various tin and germanium concentrations are demonstrated, allowing for characterization of a wide range of alloy compositions.

on *c*-sapphire have x values of 0.71 ± 0.07, 0.51 ± 0.06, 0.40 ± 0.05, and 0.37 ± 0.04, corresponding to germanium RF powers of 44 W, 74 W, 104 W, and 134 W, respectively. The films on *c*-GaN have x values of 0.88 ± 0.03, 0.81 ± 0.02, 0.61 ± 0.02, 0.50 ± 0.02, and 0.36 ± 0.01, corresponding to germanium RF powers of 30 W, 44 W, 60 W, 104 W, and 134 W, respectively. The value of x was calculated by taking the ratio of atomic percent tin to the total atomic percent of group IV elements.

3.1.2 X-ray Diffraction Studies of Phase Separation

Verification of the structure and phase of sputtered $ZnSnN_2$ (x = 1) was described in Chapter 2, and a similar examination was done to confirm that the structural properties of the $ZnGeN_2$ (x = 0) deposited here agreed with the literature. Films on *c*-GaN substrates were measured by θ-2θ XRD using copper Kα radiation (λ = 1.54 Å) over a 2θ range of 25° to 45°. The $ZnGeN_2$ films presented one prominent peak at 2θ = 34.1°, confirmed as the (002) reflection by calculations based on theoretical lattice parameters [7]. The corresponding experimental *c* lattice parameter calculated using Equation (2.1) is 5.25 ± 0.01 Å for the $ZnGeN_2$ deposited by reactive RF sputtering. This value is slightly larger than the experimental values reported in the literature, which range from 5.12 to 5.20 Å [29], and even includes measurements of other sputter deposited $ZnGeN_2$ [17]. Kikkawa *et al*. attributes the slightly larger parameter of their material to excess nitrogen incorporation during sputtering, and the same process may be involved here.

The structure of the $ZnSn_xGe_{1-x}N_2$ films was also studied using XRD to determine whether the material was a continuous alloy or if it was a mixture of different phases. Simply by switching from ternary materials to a quaternary alloy, the variability in the deposition process increases significantly. It was therefore important to ensure that other nitride or oxide phases were not being created, especially ones that would indicate phase separation of the alloys. The intermediate compositions of single phase $ZnSn_xGe_{1-x}N_2$ were expected to have XRD peaks with 2θ positions in between those of $ZnSnN_2$ and $ZnGeN_2$, in accordance with Vegard's law. On *c*-sapphire substrates, two peaks were observed in each film corresponding to the (002) and (211) or (021) reflections, meaning the films are

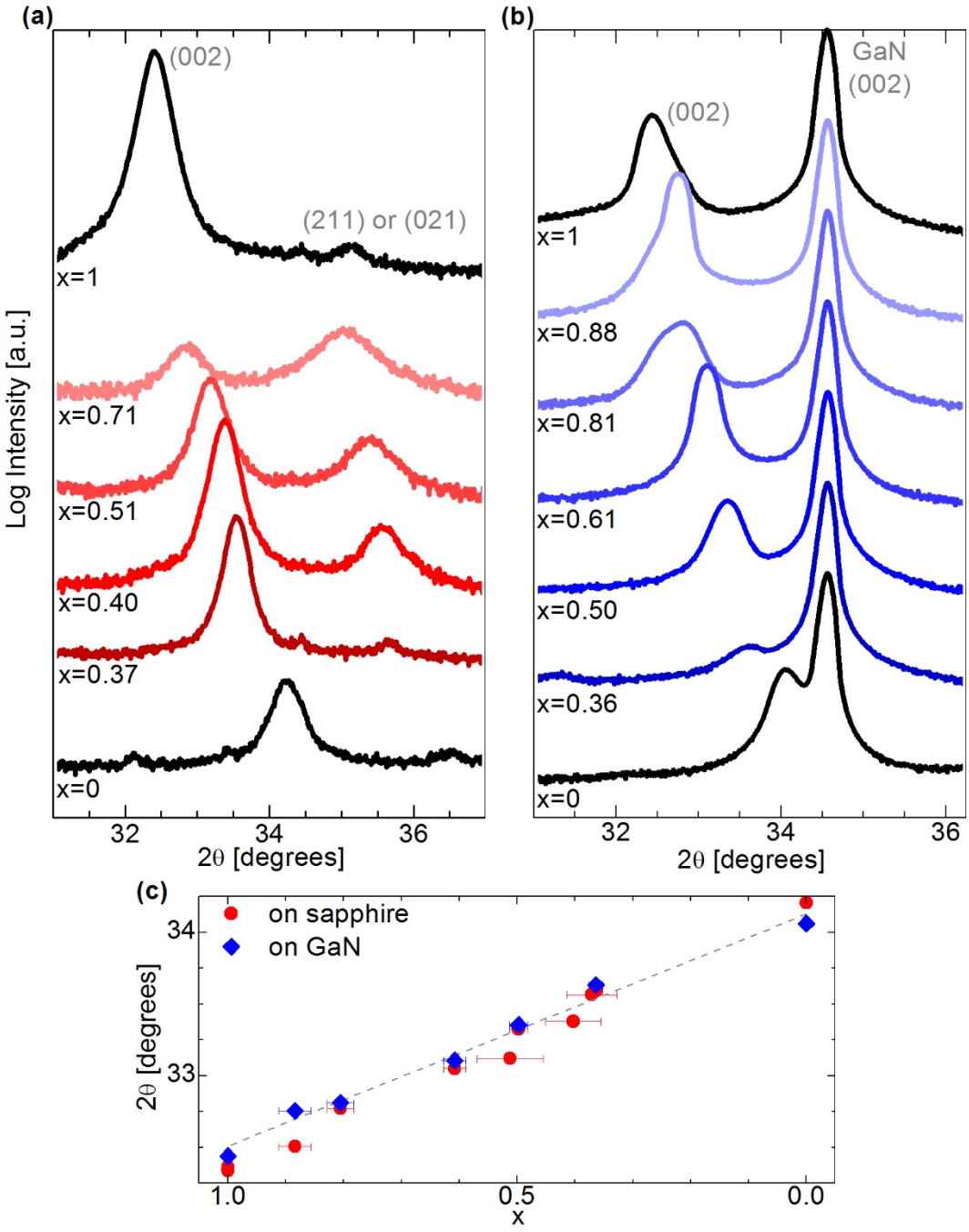

Figure 3.2. θ-2θ X-ray diffraction data from $ZnSn_xGe_{1-x}N_2$ films deposited on (a) *c*-sapphire and (b) *c*-GaN substrates. (c) All films have a prominent (002) peak whose position shifts linearly with composition, *x*. Peaks are identified by Miller indices assigned based on theoretical unit cell calculations. Error bars indicate statistical error calculated by peak-fitting software.

highly polycrystalline with the grains oriented in different directions. On *c*-GaN substrates, a strong (002) reflection coupled with weak peaks or no peaks in any other crystallographic directions indicated that the films are strongly textured with the (001) planes parallel to the surface of the substrate. Figure 3.2a-b displays the XRD θ-2θ scans around the (002) reflection for films with various compositions grown on *c*-sapphire and *c*-GaN substrates. The (002) peak position increases steadily with increasing germanium content, indicating that there is no apparent phase separation in the material. This result contrasts with $In_xGa_{1-x}N$ alloys, where the large lattice mismatch between InN and GaN causes the indium to segregate for alloys with high indium content, resulting in phase separation and formation of distinct domains of InN and GaN. An XRD measurement for phase separated $In_xGa_{1-x}N$ would therefore show two separate peaks representing the two different lattice parameters present in the material. In the $ZnSn_xGe_{1-x}N_2$ case, there is only one prominent peak in the 2θ range of the (002) reflection, and for films with $0 < x < 1$ there are no peaks at the 2θ positions of $ZnSnN_2$ or $ZnGeN_2$. This singular (002) peak reinforces the conclusion that the material is continuous and not a mixture of different phases. Additionally, the 2θ position of the (002) peak increases constantly with increasing germanium content, meaning that the unit cell continuously expands and contracts as the composition is changed such that each composition creates a unique material. This result is promising because it suggests that the entire range of bandgap values should be accessible without the need for more complicated growth strategies. Figure 3.2c further highlights the continuous alloying of the films by showing that the relationship between the (002) peak position and composition is linear. Consequently, the *c* lattice parameter decreases linearly with increasing germanium content. Data from many samples with

various compositions are shown, with a linear fit of the data for films grown on *c*-GaN. The films grown on GaN are of higher crystalline quality because the lattice mismatch between GaN and $ZnSn_xGe_{1-x}N_2$ is about half of the mismatch between sapphire and $ZnSn_xGe_{1-x}N_2$.

3.2 Optical Bandgap and Absorption Properties

The continuously shifting 2θ position of the (002) peak with changing composition, exhibited in these $ZnSn_xGe_{1-x}N_2$ thin films, essentially points to alloying of the material with no observable phase separation according to the XRD analysis. The reason the growth of these materials does not suffer from the same difficulties as $In_xGa_{1-x}N$ growth is likely because the difference in lattice parameter between $ZnSnN_2$ and $ZnGeN_2$ is about half as large as the difference between InN and GaN. Therefore, $ZnSn_xGe_{1-x}N_2$ is able to accommodate a larger range of compositions without straining the lattice to a point where phase separation is favorable. This result is valuable because it suggests that the entire range of predicted bandgaps for $ZnSn_xGe_{1-x}N_2$ should be easily accessible by tuning the ratio of the group IV elements.

To study the bulk electronic structure of these materials, spectroscopic ellipsometry measurements were made to reveal features in the joint density of states, particularly the optical absorption edge. The system, from SENTECH, uses a xenon lamp visible light source and a Fourier-transform infrared spectrometer to access wavelengths of 250 nm < λ < 2300 nm. The angle of incident light was varied between 50°, 60°, and 70° from the surface normal to improve the accuracy of the fitting algorithm. Only films grown on *c*-sapphire were measured with this method because avoiding the additional GaN layer

ensured that the fitting model was as simple as possible. Although the transparency of sapphire caused some issues involving multiple reflections, this could often be mitigated by measuring thicker films. Output data from the ellipsometer consists of the amplitude (Ψ) and phase (Δ) of the change in polarization due to interaction with the material. The wavelength-dependent refractive index (n) and extinction coefficient (k) were fit from the measured Ψ and Δ at 1 nm intervals assuming an isotropic film. $k(\lambda)$ was then used to calculate the absorption coefficient using $\alpha(\lambda) = 4\pi k(\lambda) / \lambda$. For direct bandgap semiconductors, a plot of the square of the absorption coefficient versus photon energy can be linearly extrapolated to the energy axis to estimate the value of the optical bandgap.

Because $ZnSnN_2$ was a new material, it was first important to characterize the optical properties alone before alloying with $ZnGeN_2$. An example of the extracted $n(\lambda)$ and $k(\lambda)$ data for a thick $ZnSnN_2$ film is shown in Figure 3.3. From this data, it can be shown that the material is highly absorbing, with $\alpha > 10^4$ cm^{-1} over the entire visible range.

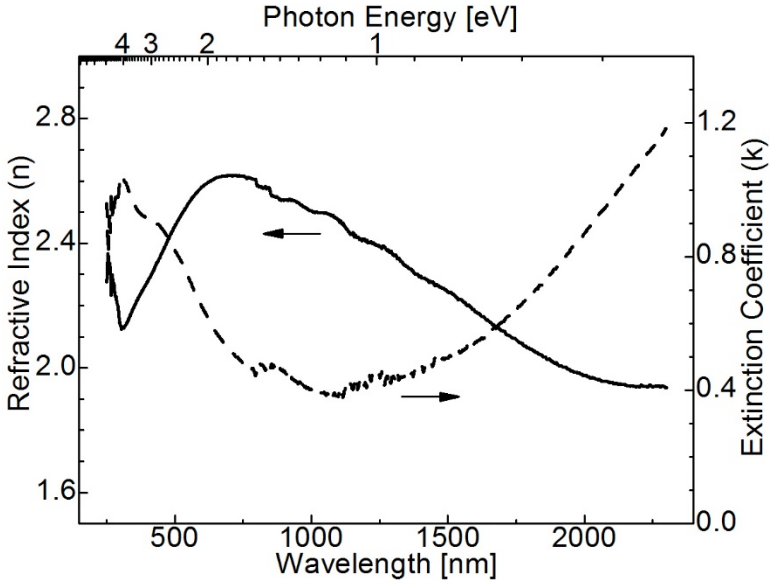

Figure 3.3. Refractive index, $n(\lambda)$, and extinction coefficient, $k(\lambda)$, extracted from spectroscopic ellipsometry measurements of a representative $ZnSnN_2$ film. $k(\lambda)$ has a minimum value greater than zero due to defect absorption.

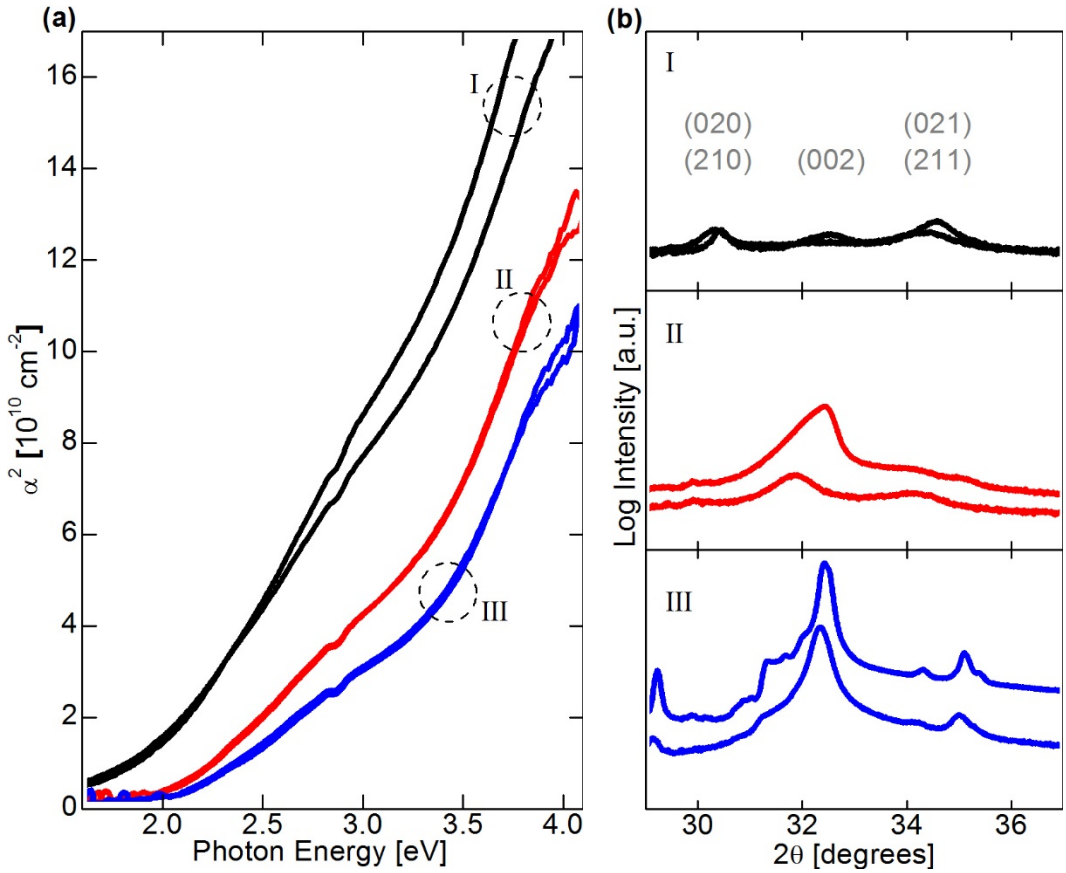

Figure 3.4. Optical bandgap estimation for $ZnSnN_2$. (a) Squared absorption coefficient vs. photon energy for six stoichiometric $ZnSnN_2$ samples. Data was linearly extrapolated near the absorption edge to estimate an optical bandgap energy of about 1.8 to 2.1 eV. (b) θ-2θ X-ray diffraction data of the same films represented in (a). Samples with similar absorption spectra also have a similar crystal structure.

It should also be noted that the extinction coefficient of the measured film never reaches zero. For an ideal material with an optical bandgap, there should be zero absorption for energies below that gap. One possible explanation for this result is that the deposited material will always exhibit a low level of defect absorption because the data in Figure 3.3 was obtained from a predominantly amorphous film. Various films with thicknesses between 1.5 and 3 μm were analyzed, and the plots of squared absorption coefficient vs.

photon energy are shown in Figure 3.4a. All samples were stoichiometric and deposited under optimized growth conditions by co-sputtering. A linear fit of the data near the absorption edge reveals a direct optical bandgap of about 1.8 to 2.1 eV. Theoretical predictions for the fundamental bandgap of $ZnSnN_2$ range from 1.4 to 2.1 eV [3-5]. One point of note in Figure 3.4a is that although the extrapolated optical bandgap values are similar, the absorption coefficients vary significantly between samples. In analyzing this further, it was discovered that the differences in absorption properties were related to the crystallinity of the material. Figure 3.4b displays the θ-2θ XRD scans of the same samples as indicated. The samples with similar absorption properties also have similar peak patterns in XRD. Additionally, the magnitude of the absorption increases as the (002) peak broadens. The exact mechanism for this effect is not known, but may be related to speculations that the degree of cation disorder can affect the bandgap of $ZnSnN_2$ [4].

The optical bandgap of the $ZnGeN_2$ deposited here was also measured to confirm agreement with literature values. The plot of squared absorption coefficient vs. photon energy for two of these samples is displayed in Figure 3.5. The oscillations in the data are most likely due to thin film interference effects as these films were less than 500 nm thick. The extrapolated optical bandgap is about 3.1 eV, which is in agreement with previous measurements of sputtered material [17]. $ZnGeN_2$ grown by other methods has reported bandgap values between 2.7 and 3.4 eV [29].

Finally, the optical bandgap extrapolations for $ZnSn_xGe_{1-x}N_2$ films with $0 < x < 1$ are shown in Figure 3.6. The absorption exhibits a blue-shift as the germanium content is increased, and is bounded by the data from $ZnSnN_2$ and $ZnGeN_2$. Like alloying between other nitride semiconductors, the shift is not linear with the change in composition. The

accuracy of these measurements is also obscured by the large band tails near the absorption edge in all of the samples. These are likely due to defect absorption, as sputter deposition is not the highest quality semiconductor growth method, and XRD measurements indicate that the films are polycrystalline. Nevertheless, the absorption varies enough with composition that accessing all of the bandgap values between 1.8 and 3.1 eV is feasible with $ZnSn_xGe_{1-x}N_2$, including the bandgap energy corresponding to green light. This suggests that the "green gap" could be closed with better control of the composition of these materials.

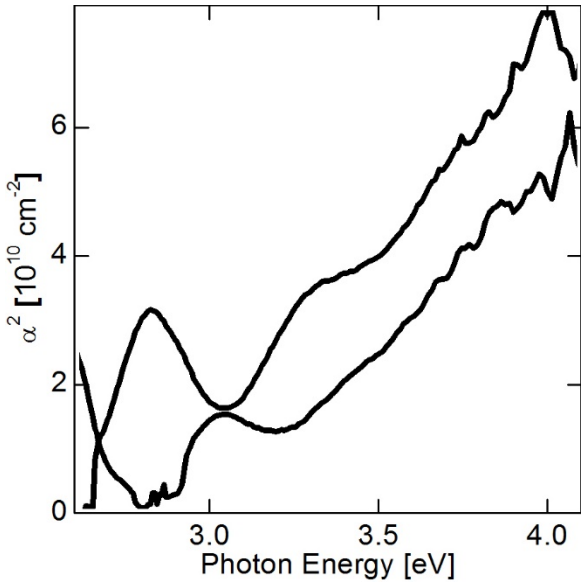

Figure 3.5. Optical bandgap estimation for $ZnGeN_2$. Squared absorption coefficient vs. photon energy for two $ZnGeN_2$ samples. Data was linearly extrapolated near the absorption edge to estimate an optical bandgap energy at about 3.1 eV.

3.3 Conclusion

Presented in this chapter is the investigation of tunable bandgap $ZnSn_xGe_{1-x}N_2$ alloys and the characterization of their optical properties. These new materials are predicted to have

optoelectronic properties that are similar to those of $In_xGa_{1-x}N$, suggesting applications as an earth-abundant alternative to current III-nitride materials.

Thin film growth of $ZnSn_xGe_{1-x}N_2$ alloys was demonstrated using reactive RF co-sputter deposition. The alloy composition (x) was varied by only changing the plasma power applied to one of the metal targets. Results from θ-2θ XRD measurements show that the (002) peak position linearly increases in 2θ with decreasing x over a wide range of compositions. Furthermore, no additional peaks were observed belonging to a different $ZnSn_xGe_{1-x}N_2$ phase or any other nitrides or oxides. The conclusion drawn from this data is that $ZnSn_xGe_{1-x}N_2$ does not phase separate in the same way that $In_xGa_{1-x}N$ does. As a result, the bandgap of $ZnSn_xGe_{1-x}N_2$ alloys should also be tunable over the entire range of x from $ZnGeN_2$ to $ZnSnN_2$. In fact, data extracted from spectroscopic ellipsometry measurements showed that the optical bandgap of the samples grown here is tunable from about 1.8 eV to 3.1 eV. This range includes the bandgap correlating to emission of green light with a wavelength of 520-530 nm, suggesting that $ZnSn_xGe_{1-x}N_2$ alloys can potentially overcome the "green gap" that has become an obstacle for traditional semiconductors. Furthermore, the exploration of additional alloy compositions would be better facilitated by more accurate bandgap measurements. If spectroscopic ellipsometry continues to be the characterization method of choice, reducing defects in the material could decrease band tails at the absorption edge, and ensuring an adequate film thickness could reduce thin film interference effects. Photoluminescence (PL) is also a common method for measuring bandgap states. Previous attempts to measure PL from these materials was unsuccessful, although Quayle *et al*. have observed PL excitation from $ZnSnN_2$ grown using a plasma assisted vapor-liquid-solid technique [20]. A fit of their PL

excitation spectra suggests a band gap of 1.7 ± 0.1 eV, while the peak in the PL spectrum is around 1.4 eV. It is unclear if the peak value is due to defect luminescence or if it represents the intrinsic band gap energy [20].

One important result that came out of this study was the measurement of the optical bandgap for $ZnSnN_2$, which had not be experimentally characterized before. Values ranged from 1.8 to 2.1 eV, and the absorption properties appeared to be strongly dependent on the crystallinity of the material. These bandgap values tend to agree with predictions made by Punya *et al*. [5] and Feldberg *et al*. [4], who both arrived at a bandgap of about 2 eV using

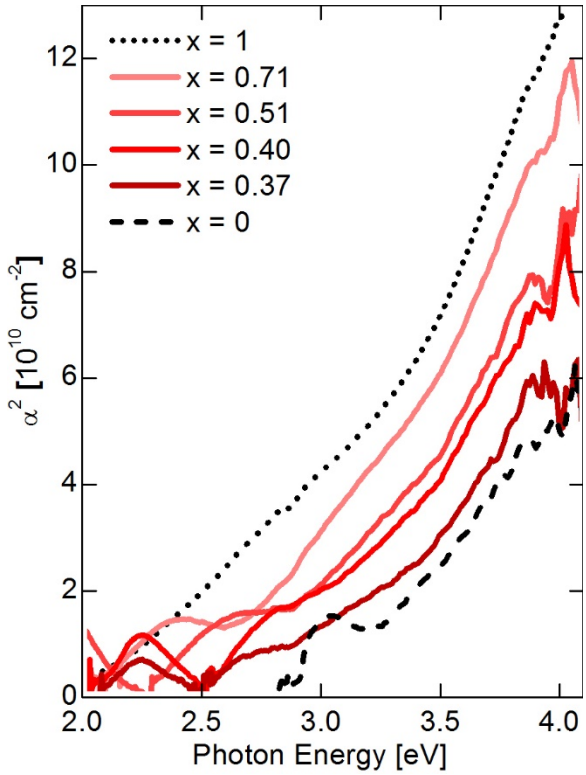

Figure 3.6. Optical bandgap estimation for $ZnSn_xGe_{1-x}N_2$ alloys. Squared absorption coefficient vs. photon energy for $ZnSn_xGe_{1-x}N_2$ samples with a range of compositions, *x*. Data was linearly extrapolated near the absorption edge to estimate optical bandgap energies that increase as *x* decreases.

density functional theory. Without any other experimental data to compare to, the best option for evaluating $ZnSnN_2$ results is to refer to the literature for InN. For many years, the accepted bandgap of InN was about 2 eV, originally observed in sputtered InN. The true fundamental bandgap of about 0.7 eV was only recently discovered by using molecular beam epitaxy, which grows a higher purity material [30]. This discrepancy is generally attributed to oxygen contamination and filling of the conduction band by excess electrons. Because $ZnSnN_2$ was also deposited by sputtering and has a predicted electronic structure similar to that of InN, the fundamental bandgap of the material may be closer to another prediction made by Lahourcade *et al*. of 1.4 eV [3]. If the bandgap is actually much lower than 2 eV, then the tunable range of $ZnSn_xGe_{1-x}N_2$ could be expanded significantly. Confirming the real bandgap, however, will require synthesis of high purity $ZnSnN_2$ by a method such as molecular beam epitaxy or metalorganic chemical vapor deposition.

The following chapter will examine the interaction between the optical and electronic properties of $ZnSn_xGe_{1-x}N_2$ alloys. In particular, investigations of the electronic structure of $ZnSnN_2$ were carried out to determine if any features could have a significant effect on the absorption edge observed with spectroscopic ellipsometry.

Chapter 4

Bulk Electronic Properties of $ZnSn_xGe_{1-x}N_2$

Good electronic properties are essential to the efficacy of semiconductor devices. Optoelectronic devices rely not only on strong interaction with light, but also on the capacity to transport charge efficiently. For devices implementing p-n junctions, the ability to dope a semiconductor is also very valuable. III-nitride materials have come to be recognized as favorable materials for such applications, mostly because they have tunable bandgaps with direct transitions. The polar wurtzite crystal structure of III-nitrides also allows for certain attributes that could be advantageous in devices such as piezoelectricity and non-linear optical properties, which are not observed in other common semiconductors like silicon and GaAs. The zinc-IV-nitride materials are predicted to have crystal and electronic structures similar to those of the III-nitrides, so the same device advantages could be expected for these new earth-abundant compound semiconductors.

Results from the previous chapter revealed that the bandgap of sputter deposited $ZnSn_xGe_{1-x}N_2$ alloys was tunable over a range of about 1.8 to 3.1 eV. Measurements also indicated that these materials are highly absorbing, although the absorption is slightly decreased as the bandgap increases. In this chapter, the $ZnSn_xGe_{1-x}N_2$ alloys are explored further by characterizing their bulk electronic properties, specifically by measuring the carrier transport properties. $ZnSnN_2$ is found to be unintentionally doped with electron

densities as high as 10^{22} cm^{-3}, likely incurring a Burstein-Moss shift. $ZnGeN_2$, on the other hand, was too resistive to make any carrier transport measurements. Discussion of the relationship between optical and electronic properties in zinc-IV-nitride materials will also be presented in this chapter to understand their potential for use in optoelectronic devices.

4.1 Making Ohmic Contacts

Electrical contacts are the method through which semiconductor materials and devices interact with external systems. Contacts can be ohmic or non-ohmic (rectifying), where ohmic contacts are defined as having a linear current-voltage relation, as described by Ohm's law. In making measurements of electronic properties, and thinking ahead towards device design, it is essential that contacts have ohmic character so as not to interfere with the behavior of the material being studied. Discovery and preparation of ohmic contacts can be a formidable task, as evidenced by the amount of research effort dedicated to the subject. The Schottky-Mott model predicts that a metal will form an ohmic contact with a given n-type semiconductor if the metal work function is less than the electron affinity of the semiconductor. Similarly, for p-type semiconductors, the metal work function much be larger than the sum of the electron affinity and bandgap of the semiconductor to make an ohmic contact. It turns out that this model does not describe real material interactions very well, but it is nonetheless a good starting point. Beyond simply choosing an appropriate metal work function, fabrication of contacts often requires deposition of multiple layers and additional annealing steps to achieve the desired ohmic behavior. For these reasons, preparation of reliable ohmic contacts is often considered an art form and is a major focus of studies on III-V device fabrication.

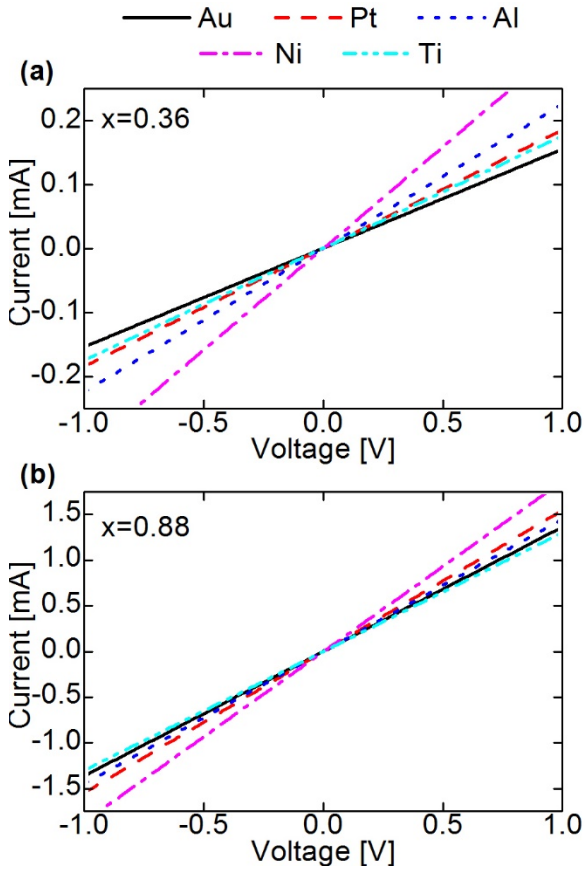

Figure 4.1. Current-voltage measurements of metal contacts on $ZnSn_xGe_{1-x}N_2$ films with compositions of (a) x = 0.36 and (b) x = 0.88. All metals make ohmic contact with the samples, indicated by linearly-shaped curves.

Common contacting metals were tested to determine if an ohmic contact could be developed for $ZnSn_xGe_{1-x}N_2$ alloys. These included gold, platinum, aluminum, nickel, and titanium. Metals were deposited by sputtering or e-beam evaporation on opposite edges of $ZnSn_xGe_{1-x}N_2$ films in preparation for measurement on a 2-point probe station. No annealing or additional preparation was performed on the contacted films. The resulting current-voltage curves from two different compositions of $ZnSn_xGe_{1-x}N_2$ are shown in Figure 4.1. All of the metals form an ohmic contact to the samples that were tested. This result suggests that $ZnSn_xGe_{1-x}N_2$ either has an electron affinity greater than 5 eV, which

is the largest metal work function tested, or a Fermi energy that lies above the conduction band edge.

The next section will discuss characterization of the carrier transport properties of $ZnSn_xGe_{1-x}N_2$ films. The results will support the hypothesis that the Fermi energy of these materials lies within the conduction band, indicative of a degenerate semiconductor.

4.2 Majority Carrier Transport Properties

The ability to transport charge efficiently is a hallmark of semiconductor materials that are widely used in device applications. To assess the suitability for optoelectronic devices, the transport properties of majority carriers in $ZnSn_xGe_{1-x}N_2$ alloys were characterized with resistivity and Hall effect measurements. Films are found to have characteristics of degenerately doped semiconductors, most likely resulting from the use of sputtering as a deposition method.

4.2.1 Resistivity Measurements

In-plane resistivity measurements were conducted on various $ZnSn_xGe_{1-x}N_2$ films using both four-point probe and van der Pauw geometries. A plot of the data is shown in Figure 4.2 as a function of the alloy composition, *x*. Resistivity was so large in $ZnGeN_2$ that no current could be passed through the samples for measurement. For all other sample compositions, the resistivity appears to increase exponentially with increasing germanium content spanning nine orders of magnitude, from 10^{-3} to 10^{5} Ω·cm. These values are somewhat lower than those of typical semiconducting materials. For example, silicon

resistivity is on the order of 10^2 Ω·cm and that of GaAs can range from 10^{-1} to 10^8 Ω·cm. The exponential relationship is likely related to the shifting electronic band structure as the composition of the alloys is varied. If the Fermi level remains at a constant energy and the conduction band increases in absolute energy with increasing germanium content, an exponential trend in resistivity would be observed.

Also consistent with the expectation for semiconducting material, results show that the resistivity of $ZnSn_xGe_{1-x}N_2$ films decreases with increasing temperature [31]. However, only films with very low tin content demonstrate the expected exponential relationship. Alloys with higher tin content exhibit a negative linear relationship between resistivity and temperature. The resistivity of metals is also known to shift linearly with temperature, although the direction of the trend is opposite to that of the $ZnSn_xGe_{1-x}N_2$ films measured here. This may indicate that the materials under investigation behave in both metallic and semiconducting manners depending on the composition and growth conditions.

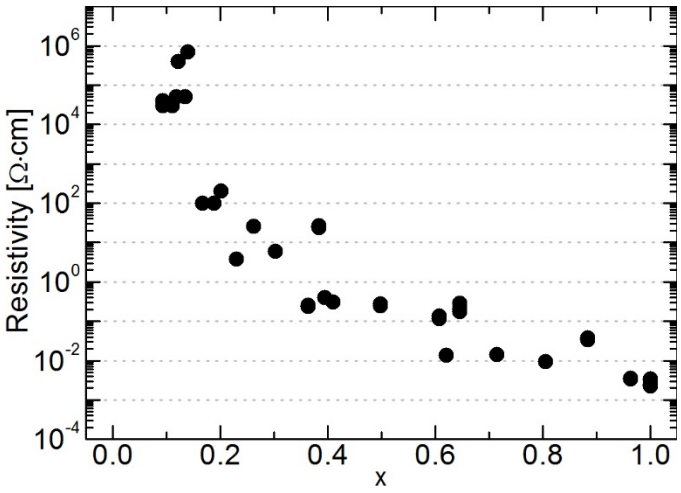

Figure 4.2. Resistivity of $ZnSn_xGe_{1-x}N_2$ films. Data was collected using four-point probe and van der Pauw geometries. Resistivity exponentially increases with increasing germanium content.

4.2.2 Carrier Density and Mobility

Hall effect measurements were used to estimate the density and mobility of bulk majority carriers in $ZnSn_xGe_{1-x}N_2$ films. Samples were cut into small squares with dimensions of approximately 6 × 6 mm, and ohmic contacts (platinum or gold) were e-beam evaporated onto the corners through a shadow mask. A schematic of the measurement geometry is shown in Figure 4.3. The prepared samples were contacted on a probe station in a van der Pauw configuration and placed into a 14000 G magnetic field. Current was flowed through contacts on opposite corners of the sample perpendicular to the magnetic field direction. The field exerts a Lorentz force on the carriers in the direction orthogonal to those of the field and current flow. Charge is then built up on opposite sides of the sample to balance

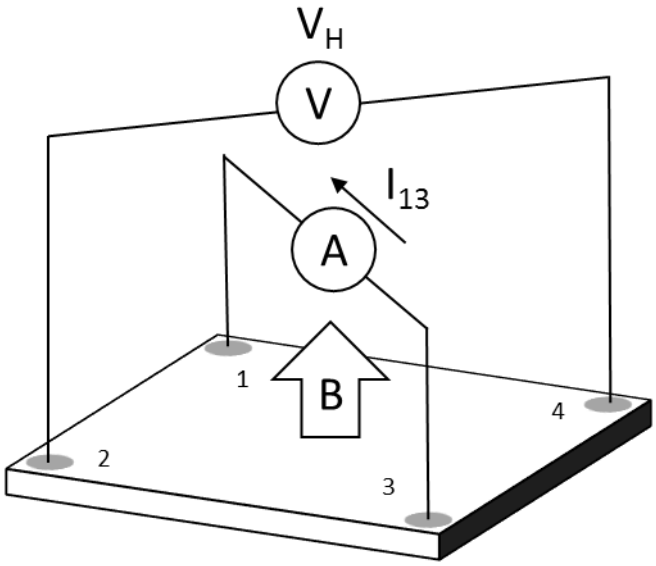

Figure 4.3. Schematic of Hall effect measurement geometry. Square samples were prepared with contacts on each corner. When current (I_{13}) is flowed through opposite corners in the presence of a magnetic field (B), a voltage (V_H) can be measured across the remaining two contacts.

the effect of the Lorentz force, resulting in a measurable voltage, or Hall voltage, across the remaining two sample contacts. The sign of the Hall voltage indicates the type of carrier being observed, and can be used to calculate the carrier mobility. Together with the van der Pauw resistivity measurements, the carrier density can also be calculated.

Results from Hall effect measurements of $ZnSnN_2$ generated very high carrier concentrations on the order of 10^{20}-10^{22} cm^{-3} with mobilities between 1 and 20 $cm^2 \cdot V^{-1} \cdot s^{-1}$, placing these materials well within the range of degenerately doped semiconductors. These results are in agreement with previous resistivity and ohmic contact experiments that indicate the sputtered $ZnSnN_2$ is essentially acting like a metal rather than a semiconductor. Measurements were also rather inconsistent in determining the carrier type, possibly because of the low mobilities or existence of multiple carrier types. However, the hot-point probe technique, where a current is measured from the flow of majority carriers away from a heat source, was utilized to show that electrons were the majority carriers.

The cause of the high unintentional doping is still unknown, but is likely related to excess defects in the material that result from the deposition method. Based on the examination of unintentional degenerate doping in InN, the leading suspects are nitrogen vacancies and oxygen impurities. In $ZnSnN_2$, an abundance of tin on zinc antisite defects could also contribute electrons to the material [32]. The mobility is likely hindered by the large carrier density due to ionized impurity scattering, but additional impedance can be caused by grain boundaries, which have been shown to act as scattering centers in InN [33]. The Hall effect only probes carrier transport that is parallel to the surface of the film. Due

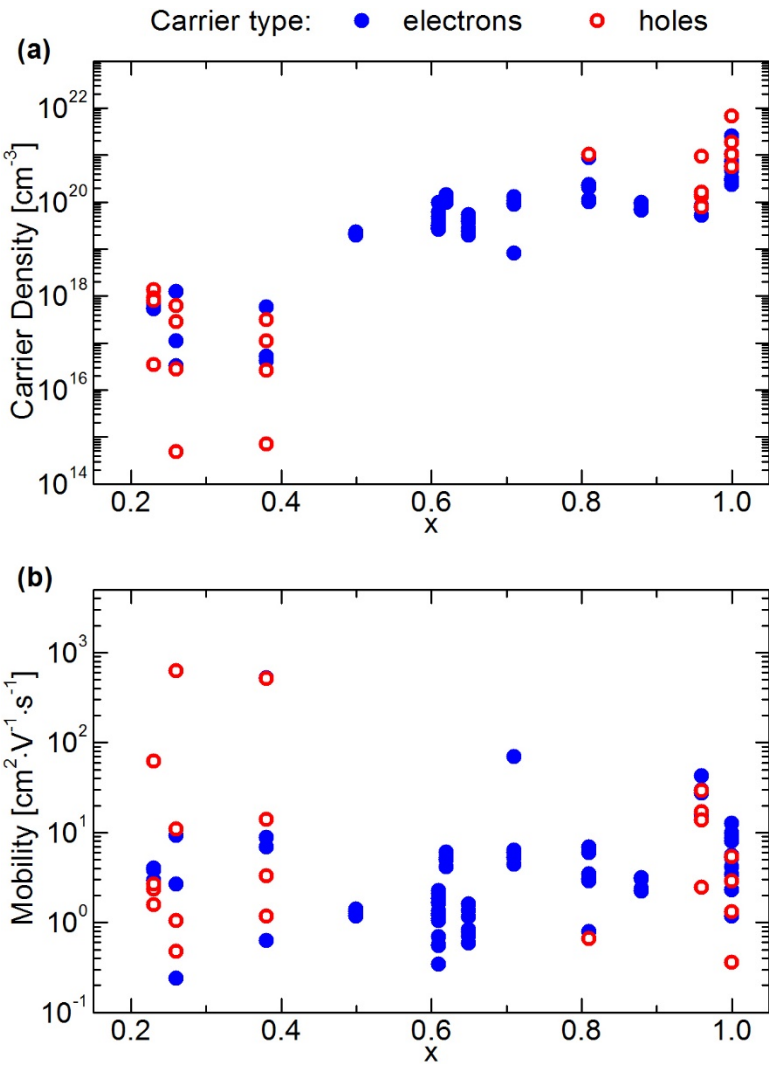

Figure 4.4. (a) Carrier density and (b) mobility for $ZnSn_xGe_{1-x}N_2$ films measured using the Hall effect. Results were inconsistent in determining the charge of the majority carriers for some compositions. Carrier density appears to decrease with increasing germanium content, but mobilities are not affected by the film composition.

to the columnar film structure, as seen in Figure 2.11, the carriers must encounter numerous grain boundaries during these Hall effect measurements.

If the observed degenerate doping is the result of the deposition method, $ZnGeN_2$ should also exhibit large carrier concentrations with low mobilities. In fact, electron concentrations of 10^{18}-10^{19} cm^{-3} were reported by Larson *et al*. with mobilities of 0.5-5 $cm^2 \cdot V^{-1} \cdot s^{-1}$ [14]. Unfortunately, the high resistivity of the sputtered $ZnGeN_2$ films studied here did not allow for accurate determination of the carrier concentrations from Hall effect measurements. However, this does suggest that there may be some composition on the spectrum of $ZnSn_xGe_{1-x}N_2$ alloys where non-degenerate behavior might be observed.

The Hall effect measurement results for various compositions of $ZnSn_xGe_{1-x}N_2$ are shown in Figure 4.4. The carrier type is still ambiguous for some of the compositions. Only films with *x* between 0.5 and 0.7 consistently reported the carrier type as electrons, with densities on the order of 10^{19} cm^{-3} and mobilities between 10^{-1} and 10^{1} $cm^2 \cdot V^{-1} \cdot s^{-1}$. These materials still behave degenerately. Overall, the carrier density does seem to decrease as the germanium content is increased, but mobilities do not appear to change with the film composition. This substantiates the claim that the low mobility is predominantly caused by the morphology of the films and grain boundary scattering rather than ionized impurity scattering from large carrier densities. As a result, growth of single crystal films or films with larger grains should show improvements in the mobility measured by the Hall effect.

4.3 Interactions between Optical and Electronic Properties

Due to the nature of the electronic structure of materials, optical properties are closely related to carrier transport. It is almost impossible to characterize one without referring to

the other. The results from the resistivity and Hall effect measurements were analyzed in the context of the bandgap studies from Chapter 3. The large electron concentrations are found to have an effect on the material's ability to absorb light. Exploration of these effects is undoubtedly important if zinc-IV-nitrides are to be implemented in optoelectronic devices.

Given the high electron carrier concentrations measured in $ZnSnN_2$, indicative of a degenerate semiconductor, observation of a Burstein-Moss shift is highly probable. As illustrated in Figure 4.5, the Burstein-Moss effect arises when free electrons fill the bottom of a semiconductor's conduction band, pinning the Fermi level to energies above the conduction band edge. This effectively blocks low-energy optical excitations from taking place, as the lowest energy states in the conduction band are already occupied. If one were to then measure the optical transitions occurring in a material exhibiting the Burstein-Moss

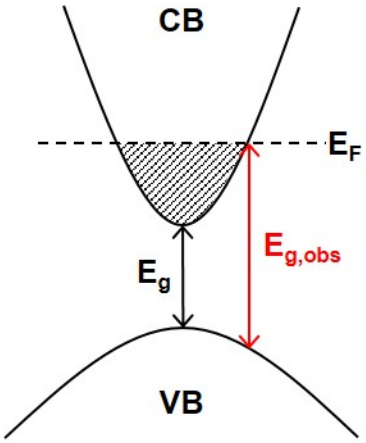

Figure 4.5. Diagram of the Burstein-Moss effect. For materials with large electron densities, the conduction band (CB) fills up and the Fermi level (E_F) is pushed into the CB. Any subsequent excitation, or observed bandgap ($E_{g,obs}$), must then occur from an energy below the valence band (VB) maximum up to E_F in the CB. $E_{g,obs}$ will be larger than the fundamental bandgap (E_g) and will be a function of carrier density.

effect, the onset of optical absorption would be observed at a larger energy than that of the underlying fundamental bandgap. This effect is exacerbated by a large curvature of the conduction band, represented by a small effective mass. The larger curvature designates that the same number of filled states will span a larger range of energies. Thus, a larger Burstein-Moss shift will be incurred in materials with a small conduction band effective mass.

From theoretical calculations of the electronic band structure, $ZnSnN_2$ is predicted to have a conduction band effective mass of as low as $0.12 \cdot m_e$ [3, 5]. Combined with the measured electron densities of up to 10^{22} cm^{-3}, a large Burstein-Moss shift can be expected in the $ZnSnN_2$ samples being studied here. Figure 4.6 presents a theoretical model for band filling in degenerate $ZnSnN_2$ assuming a parabolic conduction band and using the bandgap and effective mass values calculated in Lahourcade *et al*. The prediction does not hold at very high carrier concentrations since the actual band structure behaves linearly away from the conduction band minimum. According to the model, for electron densities around 10^{20} cm^{-3}, consistent with measured values, the effective optical bandgap is predicted to be about 2 eV. In Chapter 3, the optical absorption edge of $ZnSnN_2$ films was estimated to be between 1.8 and 2.1 eV, based on absorption data derived from spectroscopic ellipsometry measurements. These results suggest that the fundamental bandgap of $ZnSnN_2$ could be closer to 1.4 eV instead of the 2 eV being measured with optical techniques.

Once again, the InN literature was consulted here to inform on the discussion of $ZnSnN_2$. The measured bandgap of InN was initially reported as 1.9-2.1 eV, which is much larger than the currently accepted bandgap of approximately 0.7 eV. Some believe that the discrepancy could be explained by oxygen contamination, as the bandgap of In_2O_3 is about

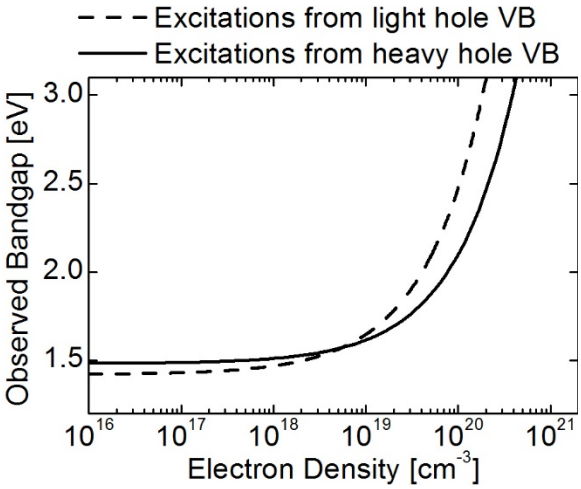

Figure 4.6. Calculated shift of the observed bandgap of $ZnSnN_2$ with the electron density due to the Burstein-Moss effect. A parabolic conduction band is assumed. Thus, the model loses validity at very high concentrations since the real band structure becomes linear away from the conduction band minimum.

3 eV, but the Burstein-Moss effect could also be the cause. Before high purity growth of InN, electron densities of ~10^{20} cm^{-3} were measured in sputtered material [34]. Additionally, InN has a very small conduction band effective mass of about $0.11 \cdot m_e$. There is now a large consensus that the previously measured bandgap of InN is primarily the result of the Burstein-Moss effect. In light of all the similarities between InN and $ZnSnN_2$, it seems unlikely that the measured optical absorption edge of about 2 eV represents the fundamental bandgap of $ZnSnN_2$. The key takeaway from our study of the history of InN is that characterization of the true bandgap will require growth of high purity material with measurable photoluminesce.

On the contrary, large Burstein-Moss shifts are not commonly observed in GaN that is not intentionally degenerately doped, which can be attributed to its larger conduction band effective mass of about $0.20 \cdot m_e$. Accordingly, $ZnGeN_2$ is predicted to also be less susceptible to band filling effects with a predicted conduction band effective mass of 0.15-

$0.22 \cdot m_e$ [5]. In fact, the measured optical bandgap for reactively sputtered $ZnGeN_2$ of 3.1 eV is only slightly larger than the theoretical value of 2.9 eV [3], and is actually less than some experimental measurements of around 3.4 eV that have been reported in the literature [13, 29]. This suggests that the magnitude of the Burstein-Moss shift will be reduced in sputtered $ZnSn_xGe_{1-x}N_2$ alloys as the germanium content is increased.

4.4 Conclusion

In this chapter, $ZnSn_xGe_{1-x}N_2$ alloys were characterized electronically. Results showed that the resistivity increased exponentially with increasing germanium content. Additionally, degenerate electron carrier densities of up to 10^{22} cm^{-3} were measured, allowing the materials to make ohmic contact to various high work function metals. The degeneracy of these materials was also related to the optical characterization from Chapter 3. Large carrier concentrations are likely to cause a Burstein-Moss shift, which would prevent direct optical measurement of the fundamental bandgap energy. Therefore, the lower end of the accessible bandgap energy range of $ZnSn_xGe_{1-x}N_2$ alloys may be extended if growth of higher purity material can be achieved that precludes the Burstein-Moss shift.

One concern with the conclusions drawn in this chapter is that it is unclear whether the large carrier densities being measured are a bulk effect or if they result from accumulation of charge at the surface of the films. A technique like capacitance-voltage (C-V) profiling can provide information about a film's doping profile. However, C-V measurements require a rectifying junction, which could not be found in this work. InN was similarly shown to have large electron carrier densities that disallowed formation of a rectifying junction with metal contacts. Instead, a KOH-based electrolyte was used as a

Schottky contact to perform C-V measurements that implicated a surface charge accumulation layer [35]. The same technique could prove to be useful in characterizing $ZnSn_xGe_{1-x}N_2$ as well.

Another issue that was encountered in these studies was the low mobility of the charge carriers, which especially affected the Hall effect measurements. Because of the nano-scale polycrystalline morphology of the sputter deposited films, the carriers encounter numerous grain boundaries when travelling in the plane of the film. To overcome this problem, films that are single crystal or made up of larger grains must be grown. However, this is not viable if sputtering remains the method of deposition. Further exploration will require a higher quality growth method, such as molecular beam epitaxy or metalorganic chemical vapor deposition. Material with better crystalline quality should also contain fewer defects than sputtered films, resulting in a decrease in the unintentional doping.

Chapter 5

Summary and Perspective

In this chapter, the findings of the work presented in this thesis will be summarized and contextualized. Areas recognized as needing improvement will also be identified with descriptions of related work in progress and suggestions for future studies. Additionally, potential applications of zinc-IV-nitride semiconductors will be discussed.

5.1 Summary of Thesis

The overall goal of this work was to determine how suitable zinc-IV-nitride semiconductors are for utilization in optoelectronic devices. Theory predicts that these materials are promising because their structural and electronic properties are similar to those of the III-nitrides, which are widely accepted as high quality materials for device applications. In addition, zinc-IV-nitride semiconductors are completely composed of earth-abundant elements, allowing for the large-scale deployment required by growing industries like solid state lighting and solar energy conversion. For these reasons, the characterization of zinc-IV-nitride semiconductors makes a positive contribution towards the advancement of sustainable technologies.

Taking into consideration the need for interactions with visible wavelengths of light, the lowest bandgap material, $ZnSnN_2$, is the most interesting. However, there were no reports in the literature of $ZnSnN_2$ synthesis at the start of this project, despite multiple reports of experimental $ZnGeN_2$ and $ZnSiN_2$ characterization. Thus, stoichiometric single phase $ZnSnN_2$ was synthesized here using reactive radio frequency (RF) magnetron sputter deposition. Composition measurements were enlisted to guide the optimization of the deposition parameters to reduce oxygen contamination and achieve a zinc/tin ratio of close to 1. The deposited material exhibited the predicted $Pna2_1$ wurtzite-derived orthorhombic crystal structure with measured lattice parameters that agree with theoretical values. Studies of the film morphology revealed small, columnar grains, typical of sputtered material. It was also discovered that the smaller lattice mismatch to GaN, compared to sapphire, allowed for growth of highly crystalline and textured $ZnSnN_2$ films that were strained at the interface.

Of relevance to applications involving interaction with light, an optical bandgap for $ZnSnN_2$ was estimated from absorption data to be between 1.8 and 2.1 eV. The absorption properties also appeared to depend strongly on the crystallinity of the films. These bandgap values are in agreement with some theory predictions [4, 5] and with more recent experimental results [4, 20]. However, in exploring the carrier transport properties of $ZnSnN_2$, degenerate electron densities of up to 10^{22} cm^{-3} were measured. Large carrier concentrations, in concert with a small predicted conduction band effective mass, are very likely to induce a Burstein-Moss shift. Such a shift would prevent direct optical measurement of the fundamental bandgap energy, suggesting that the fundamental bandgap of $ZnSnN_2$ is much less than 1.8 eV.

To expand the potential range of applications for zinc-IV-nitride semiconductors, a tunable bandgap would be of great value. To this end, germanium was incorporated into the $ZnSnN_2$ deposition process to yield $ZnSn_xGe_{1-x}N_2$ alloys with a wide range of compositions, *x*. Lattice measurements indicate that these alloys follow Vegard's law and show no evidence of unwanted phases or compounds, indicating that there is no phase separation of $ZnSn_xGe_{1-x}N_2$. Furthermore, the optical bandgap derived from absorption data was shown to be tunable from about 1.8 to 3.1 eV. This range includes the bandgap correlating to emission of green light with a wavelength of 520-530 nm, suggesting that $ZnSn_xGe_{1-x}N_2$ alloys can potentially overcome the "green gap" that has become an obstacle in the solid state lighting industry. If the fundamental bandgap of $ZnSnN_2$ is found to be much lower than 1.8 eV, due to a Burstein-Moss shift, the lower end of the accessible bandgap energy range of $ZnSn_xGe_{1-x}N_2$ alloys may be extended further.

5.2 Current and Future Work

Throughout the previous chapters, there were many discussions about the areas where improvements could be made to better understand the fundamental properties of zinc-IV-nitride materials. In addition to limitations on equipment capability and availability, many characterization techniques require previous knowledge of some material properties. As these materials are not very well-studied, confirmed material parameters were in short supply. Ultimately, the work completed here only lays the groundwork for further studies of zinc-IV-nitride semiconductors in the future. The following is a discussion of the areas identified where advances could be made, including some work in progress and suggestions

for future efforts. Hopefully, this can serve as a roadmap towards a thorough characterization of these promising materials.

5.2.1 Material Synthesis

One key area that was noted in all of the previous chapters was that a deposition method enabling growth of better crystalline quality material would greatly benefit the evaluation of zinc-IV-nitride semiconductors. Sputter deposition is inherently limited in its ability to form large crystals due to low surface mobility of atoms and surface damage caused by the energetic ions. Still, there are some ways to try to increase grain size and reduce impurities in sputtered films.

For the $ZnSnN_2$ synthesis, reducing defects is especially important for characterizing the intrinsic properties of this relatively new material. One method for improving the crystalline quality is to increase the substrate temperature during growth, allowing for more surface mobility. This is not a practical approach for deposition from a single mixed Zn_xSn_{1-x} target because the temperature for stoichiometric growth is tied to the target composition. However, high-temperature deposition could be advantageous for co-sputtering since the metal ratios can be controlled independently. Higher temperatures may also reduce the number of nucleation sites on the substrate surface, thus reducing the number of grains in the film. Some initial attempts at co-sputtering with substrate temperatures above 300 °C have proven to be difficult in achieving the desired stoichiometry. However, only a few conditions were tested and a more systematic study could point to more fitting deposition parameters.

A more favorable route to improving the quality of $ZnSnN_2$ may be to use a completely different technique instead of sputter deposition. Molecular beam epitaxy

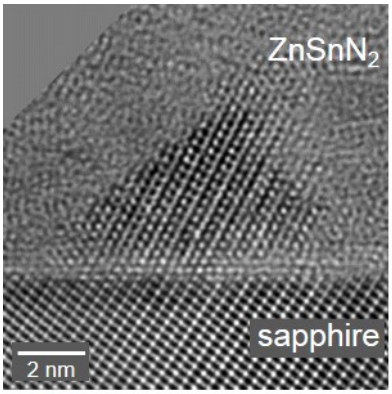

Figure 5.1. High resolution transmission electron microscope image of interface between $ZnSnN_2$ film grown by molecular beam epitaxy and sapphire substrate. Representative domain of highly ordered material is shown with some relationship to the substrate lattice.

(MBE) and metalorganic chemical vapor deposition (MOCVD) are currently the state-of-the-art growth methods for high quality semiconductor thin films. There are a few reports in the literature of initial investigations into MBE-grown $ZnSnN_2$ [4]. However, the bandgap, carrier density, and mobility values reported are similar to the ones measured here for sputtered films, even though the MBE-grown films are purportedly single crystalline. Following from the sputtering work described here, a dedicated MBE chamber is being brought up to grow high quality zinc-IV-nitride films. Trial material that has been grown thus far has a similar morphology to the sputtered films. However, transmission electron microscopy (TEM) of one sample revealed small domains of highly ordered material at the surface of the sapphire substrate, which is suggestive of the potential for higher quality growth (Figure 5.1).

Looking beyond just $ZnSnN_2$ growth, there is much room for improvement in sputter deposition of $ZnSn_xGe_{1-x}N_2$ alloys. Co-sputtering from mixed $Zn_{0.75}Sn_{0.25}$ and elemental germanium targets limits the range of attainable compositions, as the sputter

yield of tin is always linked to that of zinc. After acquiring a third RF power supply for the sputtering system, some initial studies of three-target co-sputtering from elemental targets were carried out. However, achieving the desired stoichiometry proved to be difficult because of the increase in variables. Still, having independent control of the different elements will surely be beneficial in future work for facilitating access to the entire range of $ZnSn_xGe_{1-x}N_2$ alloys and precisely tuning the bandgap.

5.2.2 Silicon-Containing Compounds

The results presented in this thesis focused on tin- and germanium-containing compounds. However, some initial work has also been completed on the silicon-containing materials. The literature contains some reports of alloying $ZnGeN_2$ with $ZnSiN_2$, but silicon could also be incorporated into $ZnSnN_2$ with an even wider bandgap range. However, $ZnSn_xSi_{1-x}N_2$ alloys may be more prone to phase separation as the lattice constant

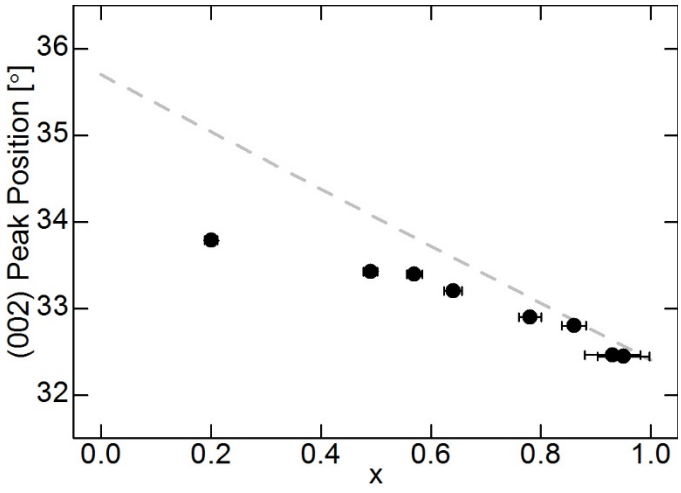

Figure 5.2. Shift of (002) X-ray diffraction peak position with composition for $ZnSn_xSi_{1-x}N_2$ films. Dashed line follows Vegard's law assuming a $ZnSiN_2$ peak position of 35.7° [2].

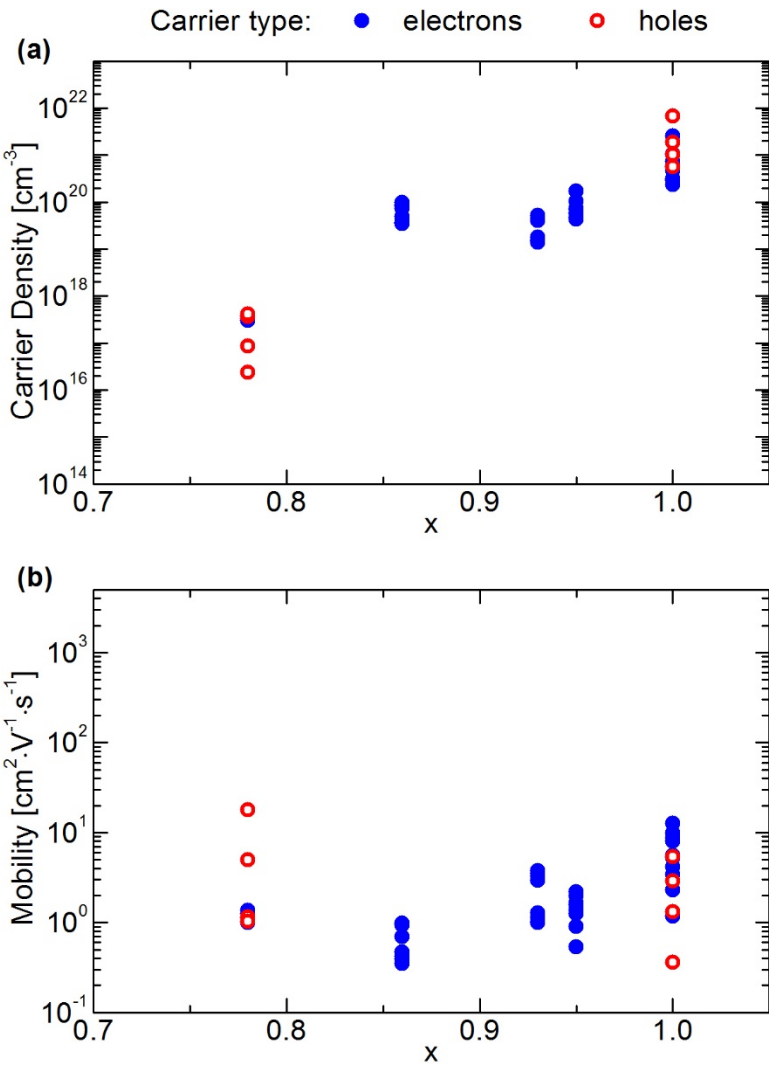

Figure 5.3. (a) Carrier density and (b) mobility for $ZnSn_xSi_{1-x}N_2$ films measured using the Hall effect. Results were inconsistent in determining the charge of the majority carriers for some compositions. Carrier density appears to decrease with increasing germanium content, but mobilities are not affected by the film composition.

difference is also much larger between the constituent compounds. Attempts were made to synthesize $ZnSn_xSi_{1-x}N_2$ alloys by sputtering from $Zn_{0.75}Sn_{0.25}$ and silicon targets. The range of compositions was inhibited by the very low sputter yield of the silicon target. It was therefore fairly easy to create low silicon alloys, but films with low tin content were not possible with the available instrumentation. Furthermore, attempts to synthesize $ZnSiN_2$ only resulted in amorphous films, precluding any lattice parameter measurements. If the lattice parameters from literature are assumed, X-ray diffraction (XRD) measurements would indicate that the alloys do not follow Vegard's law (Figure 5.2).

Hall effect measurements were also conducted on the $ZnSn_xSi_{1-x}N_2$ alloys to look for a decrease in the excess carrier concentration. The same trend seen in $ZnSn_xGe_{1-x}N_2$ films was observed here, but with a larger variation in density for the same *x*, which is expected because the bandgap changes more rapidly with composition in $ZnSn_xSi_{1-x}N_2$ (Figure 5.3a). The mobility values were also in the same range as in the other zinc-IV-nitrides, again confirming that the low mobility is primarily impacted by the film morphology and not the composition (Figure 5.3b).

5.2.3 Point Defects

Attempts at reducing the degeneracy of these materials has mostly been based on speculations about the possible sources of excess carriers as they relate to the quality of the films. Instead, a more directed approach could be developed by studying the actual defects present in the material. Some theoretical work has been reported that suggests certain point defects are contributing to the high carrier concentrations in $ZnSnN_2$, including nitrogen vacancies, oxygen impurities, and tin on zinc antisite defects [32]. To test for these defects,

a technique like positron annihilation spectroscopy could be enlisted to study vacancies. Simple composition measurements can also implicate certain defects if the resolution is high enough. TEM could also be used to study defects if their concentrations are low enough to be able to distinguish them from one another. Once the source of the degeneracy is identified, the growth procedures can be altered for reduction of particular defects.

5.2.4 Improving Measurement Capabilities

There remains a certain degree of uncertainty in the characterization that was carried out here. For example, there has been quite a bit of debate in the literature about the real crystal structure of zinc-IV-nitride semiconductors. Various reports have strongly claimed that the unit cell is monoclinic, orthorhombic, or hexagonal, even though they are all only slight distortions of one another. An accurate measurement of the lattice parameters would require a high quality crystal that is not distorted by strain. Even with the present material, additional high resolution XRD studies could be conducted to search for weak peaks that are only present in the $Pna2_1$ structure to be able to differentiate between unit cell types. Raman spectroscopy could also provide information about the ordering of the different atoms in the unit cell. Nevertheless, identifying the space group of the materials is not necessary for applications, as long as the optoelectronic properties are well-characterized.

Determination of the bandgap is another area where more accurate measurements are needed, since deriving absorption spectra from ellipsometry involves many assumptions. The model used for fitting the data was very simplistic and did not account for surface roughness or multiple reflections. Nowadays, there are more accurate models available that could provide reliable information using this method. Photoluminescence

(PL) spectroscopy is also a great technique for observing the optical transitions in a material. However, no PL was observed in sputtered $ZnSn_xGe_{1-x}N_2$ films. Improvements in material quality should allow for measurement of PL in the future. Accurate measurements of the bandgap as well as composition are required to be able to control the tuning of these alloys.

In this work, composition measurements were made by energy dispersive X-ray spectroscopy (EDXS), which is not very accurate for lighter elements. Instead, secondary ion mass spectrometry (SIMS) or Rutherford backscattering spectrometry (RBS) may be able to provide more accurate determination of the nitrogen and oxygen concentrations. This would be especially useful in identifying point defects that might be contributing to the degenerate carrier concentration. Precise zinc and group IV element compositions would also allow for the improved control of bandgap tuning alloyed materials.

Finally, carrier transport measurements require a great deal of improvement in characterizing zinc-IV-nitride semiconductors. Hall effect measurements were not even able to consistently designate the sign of the majority charge carriers. One explanation is that there are actually multiple carrier types with individual concentrations and mobilities. For example, electrons and holes may behave very differently within grain boundaries compared to the bulk crystal. Methods exist for analyzing data from magnetic field dependent Hall effect measurements that can distinguish between different carrier types. Another interesting option would be to try measuring carrier transport in a direction perpendicular to the plane of the film. However, this would likely require contacting the top and bottom of the film, as well as etching on the nitride material.

5.3 Benefit of Unintentional Degenerate Doping

Throughout this thesis, the topic of degenerate doping was mentioned many times. The context was always that degenerate doping needed to be reduced to be able to characterize the properties of the intrinsic materials. Carrier densities in the zinc-IV-nitrides grown by sputter deposition are not likely to be reduced significantly, so perhaps it would be sensible to consider how the degeneracy can work in our favor. One idea is to use the low resistivity of $ZnSnN_2$ (~10^{-3} Ω·cm) to make low temperature contacts for other semiconductors. For comparison, the resistivity of ITO is generally reported on the order of 10^{-4} Ω·cm. Even though $ZnSnN_2$ is not as transparent as ITO in the visible wavelength range, a very thin film could still act as a transparent contact for visible light. Some compositions of $ZnSn_xGe_{1-x}N_2$ may also serve as transparent contacts since the bandgap can be increased even though the resistivity stays relatively low. Thus, sputtered zinc-IV-nitrides may be able to serve as earth-abundant contacts for other semiconductor devices.

5.4 Closing Remarks

The work presented here should only be considered as the tip of the iceberg for understanding earth-abundant semiconductors. Although some major strides were made, such as demonstrated synthesis of $ZnSnN_2$ and a tunable bandgap alloy, there are still many aspects of semiconducting properties and device design that will need to be considered. Most materials take decades to be characterized well enough for successful use in device applications, and zinc-IV-nitride semiconductors will not likely be an exception. However, with some progress towards improving film quality, these materials are still very promising

for optoelectronic device applications. Hopefully this thesis can serve as a starting point for further efforts in developing zinc-IV-nitrides semiconductors.

Appendix

Attempted Synthesis by Pulsed Laser Deposition

Pulsed laser deposition (PLD) was a natural starting point for synthesizing a new compound semiconductor mainly because of its ability to stoichiometrically transfer material from a bulk target into a thin film on a substrate. PLD uses short laser pulses to ablate material from the surface of a target, which then travels through the vacuum chamber and condenses on a substrate. The laser ablation event creates a plume of various particles resulting from ionization, evaporation, and melting of the target. For the system used in this study, depicted in Figure A.1, the deposition can be altered by varying the energy and pulse frequency of the laser, the gas composition and pressure, and the substrate temperature. In general, the energy was kept at 300 mJ with a pulse frequency of 10 Hz. The strategy for growing $ZnSnN_2$ by PLD was to start with a $Zn_{0.5}Sn_{0.5}$ alloy target and incorporate nitrogen by introducing ammonia (NH_3) gas into the heated vacuum chamber during deposition. NH_3 is commonly used in III-nitride growth where the gas molecules are thermally cracked at the substrate surface. Pressed powder targets with the desired composition were acquired from ACI Alloys, Inc. with 99.99% purity and *c*-plane sapphire was chosen as a substrate due to its wide use in growth of III-nitride materials. To test the viability of using this technique, samples were prepared using various substrate temperatures and NH_3 pressures. Scanning electron microscope (SEM) images of these

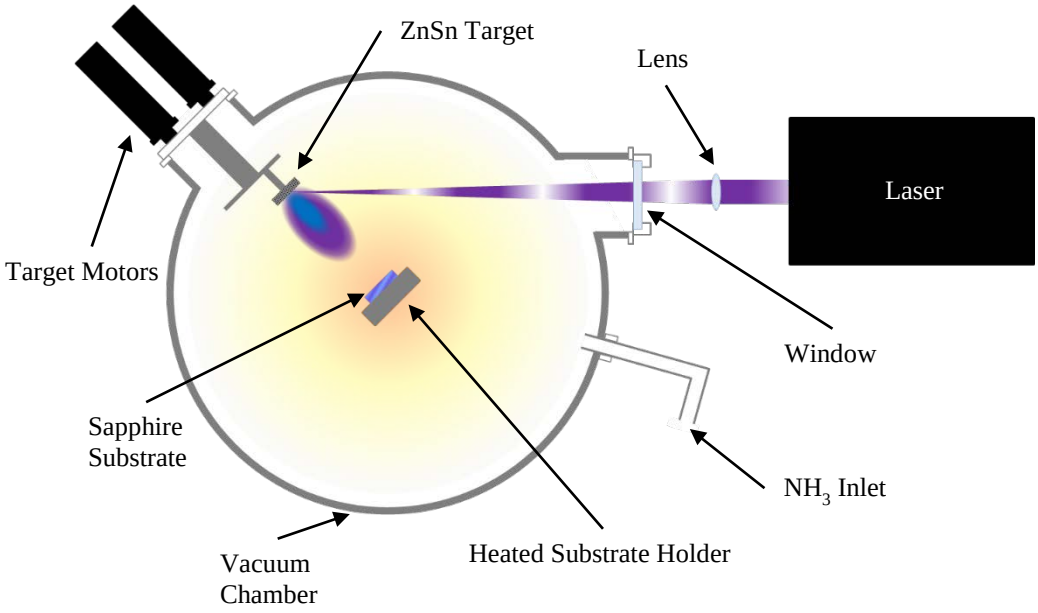

Figure A.1. Schematic of pulsed laser deposition. Short laser pulses ablate the target material and resulting particles travel through the vacuum chamber to condense on the substrate.

samples were taken along with the energy dispersive X-ray spectroscopy (EDXS) scans to characterize the surface of the deposited material, as well as X-ray diffraction (XRD) to evaluate the crystal structure.

The results revealed that samples deposited at various temperatures and a constant low pressure of about 6 mTorr exhibited differences in the surface morphology. Figure A.2 shows that as the temperature is increased from 30 °C to 650 °C, excess tin on the surface of the substrate tends to bead up and then coalesce into larger particles. These particles are poorly adhered to the substrate and can easily be rubbed off. The XRD spectra for samples at all temperatures show only peaks representing multiple orientations of tin, but EDXS indicated a small amount of zinc is present in the 30 °C and 100 °C samples. There was no indication of nitrogen incorporation in any of these samples. Furthermore, when the gas

pressure was varied up to 55 mTorr under a constant temperature of either 30 °C or 650 °C, there was no significant difference in the surface morphology or composition between samples. It became apparent that the conditions tested so far were not sufficient for cracking the NH_3 to ensure incorporation of nitrogen in the deposited material. To remedy this, a substrate nitridation step was added to the beginning of the deposition. The substrate was heated to a temperature of 750 °C, 800 °C, 900 °C, or 950 °C and left for 30 min in 6 mTorr of NH_3 before the laser was turned on. The purpose of the high temperature nitridation step is to form a thin nitride layer on the surface of the substrate that facilitates growth of subsequent nitride material. XRD spectra from these samples are shown in Figure A.3 and contain peaks that correspond to lattice spacings of not only tin, but also of

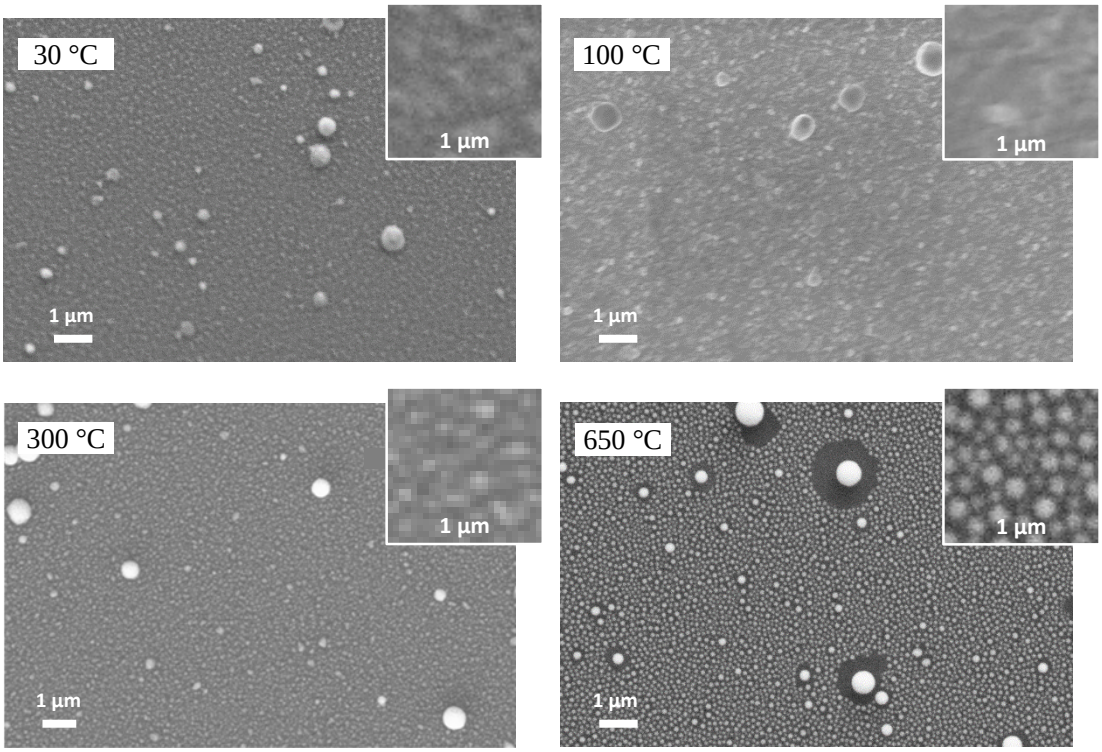

Figure A.2. Scanning electron microscope images of the sample surface when temperature is varied. As the substrate temperature increases, tin beads form on the surface.

tin nitride (Sn_3N_4) and tin oxide (SnO_2). Additionally, the EDXS results indicate the presence of nitrogen in the deposited material. Based on these findings, the importance of the high temperature nitridation step was confirmed, although it conflicts with the low temperature requirement for zinc deposition.

It became apparent that there were two competing processes that needed to be balanced for successful synthesis of $ZnSnN_2$. On one hand, the high vapor pressure and low sticking coefficient of zinc requires the use of low temperatures (< 300 °C) during deposition, but on the other hand, NH_3 cracking calls for very high substrate temperatures (> 700 °C). This led to the idea of using a two-stage growth method. First, high temperature nitridation of the substrate was performed at 800-900 °C in 6 mTorr of NH_3 and followed

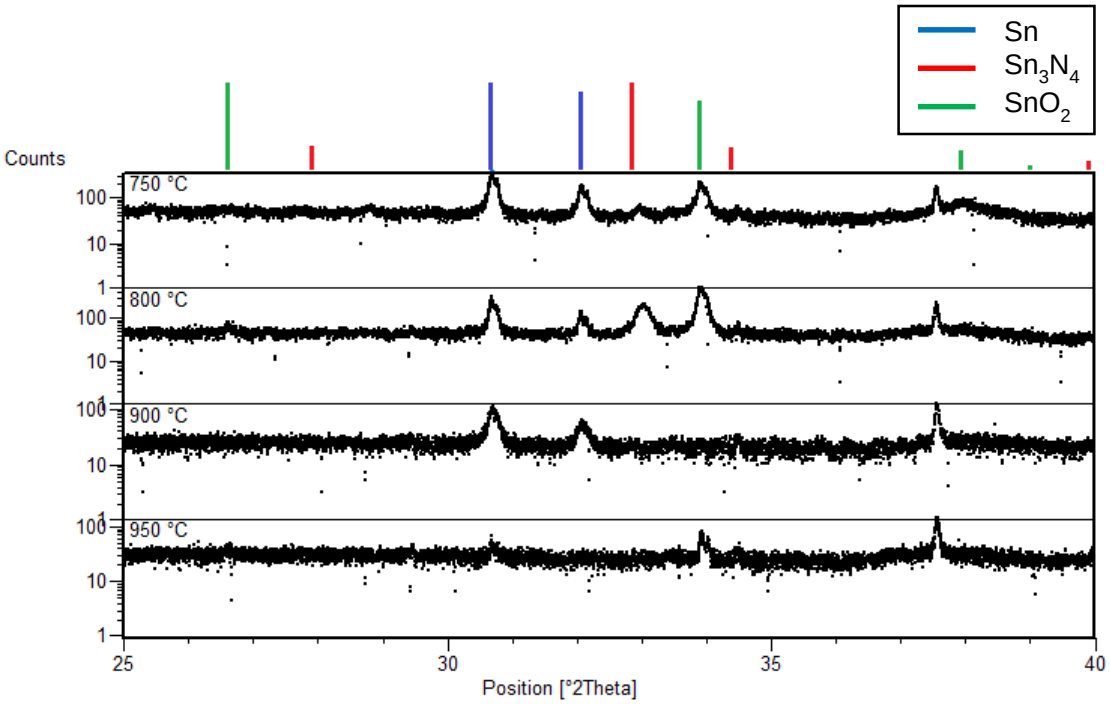

Figure A.3. θ-2θ X-ray diffraction data from samples that underwent a high temperature nitridation before deposition, resulting in nitrogen incorporation in the tin surface particles.

by PLD at room temperature or 200 °C with the hope that zinc could react with the already nitridated surface. However, XRD spectra only showed peaks for tin metal, indicating that the nitridation does not remain when the temperature is reduced. Next, the opposite approach was attempted. PLD at 200 °C was followed by continuing deposition during a temperature ramp in 6 mTorr of NH_3 up to 800-900 °C at a rate of 20 °C · min^{-1}. In this case, the zinc desorbed from the substrate during the temperature increase, again leaving beads of tin nitride on the surface. Lastly, an attempt was made to take advantage of the nitrogen plasma source in the sputtering chamber to avoid high temperatures during deposition. Zinc and tin were deposited by PLD at room temperature, and the sample was then inserted into the sputtering chamber and subjected to a nitrogen plasma with a power of 10 W for two hours. Characterization of the sample did not show any changes in XRD peaks or composition after exposure to the plasma.

As a completely different approach, the effect of changing the nitrogen source material was investigated. In the literature, nitride growth has been achieved using N_2 gas at a pressure of > 30 mTorr and substrate temperatures of 500-700 °C [36]. The concern with using high gas pressures in the PLD is that the path length of the particles in the plume is reduced so that less material is likely to reach the substrate. A visual analysis of the plume size indicated that for the $Zn_{0.5}Sn_{0.5}$ target, the plume appeared to reach the substrate surface at up to 200 mTorr. However, test samples at a substrate temperature of 200 °C resulted in very few beads of zinc and tin on the surface at a pressure of 75mTorr, and even fewer beads of only tin at a pressure of 150 mTorr. Due to the slow deposition rate at high N_2 pressures, subsequent test samples were limited to 35 mTorr. To test the use of N_2 gas, a sapphire substrate was heated to 900 °C in 35 mTorr of N_2 and PLD occurred during the

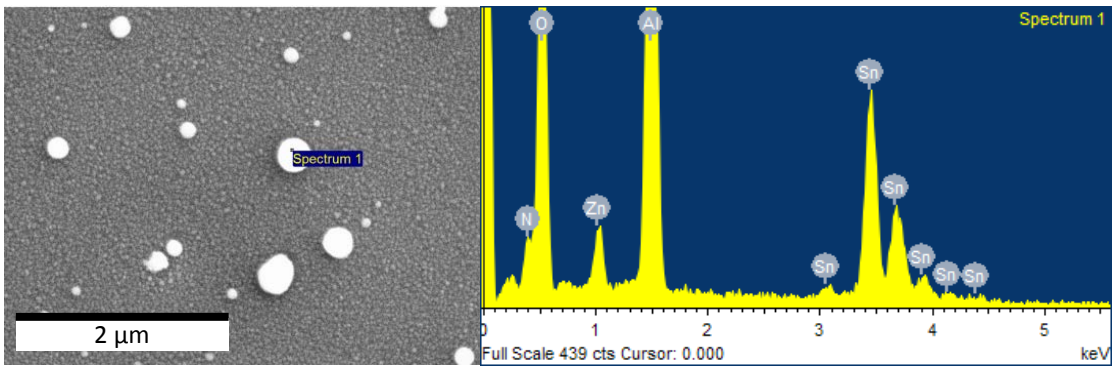

Figure A.4. Scanning electron microscope image and corresponding composition measurement by energy dispersive X-ray spectroscopy showing the presence of zinc, tin, and nitrogen in the sample.

ramp down to room temperature at a rate of 20 °C · min^{-1}. The resulting material appears to be a continuous film with particles on the surface as shown in Figure A.4. EDXS analysis revealed that the continuous film is comprised of zinc and the beads contain tin nitride. Even though all of the necessary elements for $ZnSnN_2$ are present in this sample, there is still no interaction between zinc and nitrogen.

Using PLD to synthesize $ZnSnN_2$ turned out to be very challenging and the optimization of the deposition parameters was not achieved. Striking a balance between the high temperatures required for NH_3 or N_2 cracking and the low temperatures needed for zinc adsorption became the major obstacle in this endeavor. One parameter that would have been interesting to test is the distance between the target and the substrate. With a shorter distance, the interaction between particles in the plume is closer to the deposition surface. Unfortunately, this parameter was not adjustable in the available PLD equipment. For these reasons, the focus of $ZnSnN_2$ synthesis was shifted to use of reactive sputtering, which easily provides a source of reactive nitrogen at any temperature.

Bibliography

1. Delaney, K.T., S.K. Shukla, and N.A. Spaldin, *in preparation*. 2011.

2. Endo, T., et al., *High-pressure synthesis of new compounds, $ZnSiN_2$ and $ZnGeN_2$ with distorted wurtzite structure.* Journal of Materials Science Letters, 1992. **11**(7): p. 424-426.

3. Lahourcade, L., et al., *Structural and optoelectronic characterization of RF sputtered $ZnSnN_2$.* Adv Mater, 2013. **25**(18): p. 2562-6.

4. Feldberg, N., et al., *Growth, disorder, and physical properties of $ZnSnN_2$.* Applied Physics Letters, 2013. **103**(4): p. 042109.

5. Punya, A., W.R.L. Lambrecht, and M. van Schilfgaarde, *Quasiparticle band structure of Zn-IV-N_2 compounds.* Physical Review B, 2011. **84**: p. 165204.

6. Shaposhnikov, V.L., et al., *Structural, electronic and optical properties of II–IV–N_2 compounds (II = Be, Zn; IV = Si, Ge).* physica status solidi (b), 2008. **245**(1): p. 142-148.

7. Paudel, T.R. and W.R.L. Lambrecht, *First-principles study of phonons and related ground-state properties and spectra inZn-IV-N_2 compounds.* Physical Review B, 2008. **78**: p. 115204.

8. Limpijumnong, S., S.N. Rashkeev, and W.R.L. Lambrecht, *Electronic Structure and Optical Properties of $ZnGeN_2$.* MRS Internet J. Nitride Semicond. Res., 1999. **4S1**: p. G6.11.

9. Osinsky, A., et al., *New Concepts and Preliminary Results for SiC Bipolar Transistors $ZnSiN_2$ and $ZnGeN_2$ Heterojunction Emitters.* Proc. of the IEEE/Cornell Conference on High Performance Devices, 2000: p. 168-172.

10. Cloitre, T., A. Sere, and R.L. Aulombard, *Epitaxial growth of $ZnSiN_2$ single-crystalline films on sapphire substrates.* Superlattices and Microstructures, 2004. **36**: p. 377-383.

11. Mintairov, A., et al., *Infrared spectroscopy of $ZnSiN_2$ single-crystalline films on r-sapphire.* Appl. Phys. Lett., 2000. **76**: p. 2517-2519.

12. Pearton, S.J., et al., *Magnetic and structural characterization of Mn-implanted, single-crystal $ZnGeSiN_2$.* Journal of Applied Physics, 2002. **92**(4): p. 2047-2051.

13. Du, K., et al., *Synthesis and characterization of $ZnGeN_2$ grown from elemental Zn and Ge sources.* Journal of Crystal Growth, 2008. **310**(6): p. 1057-1061.

14. Larson, W.L., H.P. Maruska, and D.A. Stevenson, *Synthesis and Properties of $ZnGeN_2$.* J. Electrochem. Soc., 1974. **121**: p. 1673-4.

15. Viennois, R., et al., *Prospective investigations of orthorhombic $ZnGeN_2$ synthesis , lattice dynamics and optical properties.* Mat. Sci. Eng. B-Solid, 2001. **82**: p. 45-49.

16. Peshek, T.J., et al., *Vibrational modes in$ZnGeN_2$: Raman study and theory.* Physical Review B, 2008. **77**: p. 235213.

17. Kikkawa, S. and H. Morisaka, *RF-sputter deposition of Zn–Ge nitride thin films.* Solid State Commun., 1999. **112**: p. 513-515.

18. Misaki, T., et al., *Epitaxial growth and characterization of $ZnGeN_2$ by metalorganic vapor phase epitaxy.* Journal of Crystal Growth, 2004. **260**(1-2): p. 125-129.

19. Zhu, L.D., et al., *Epitaxial Growth and Structural Characterization of Single Crystalline $ZnGeN_2$.* MRS Internet J. Nitride Semicond. Res., 1998. **4**: p. G3.8.

20. Quayle, P.C., et al., *Synthesis, lattice structure, and band gap of $ZnSnN_2$.* MRS Communications, 2013: p. 1-4.

21. Feldberg, N., et al., *Growth of $ZnSnN_2$ by Molecular Beam Epitaxy.* Journal of Electronic Materials, 2014. **43**(4): p. 884-888.

22. Wintenberger, M., M. Maunaye, and Y. Laurent, *Groupe spatial et ordre des atomes de zinc et de germanium dans $ZnGeN_2$.* Mat. Res. Bull., 1973. **8**: p. 1049-1054.

23. Maunaye, M. and J. Lang, *Preparation et Proprietes de $ZnGeN_2$.* Mat. Res. Bull., 1970. **5**: p. 793-796.

24. Feldberg, N., et al., *$ZnSnN_2$ A New Earth-Abundant Element Semiconductor for Solar Cells.* Proc. of the 38th IEEE Photovoltaic Specialists Conference, 2012: p. 2524-2527.

25. Misaki, T., et al., *Optical properties of $ZnGeN_2$ epitaxial layer.* physica status solidi (c), 2003. **0**(7): p. 2890-2893.

26. Misaki, T., et al., *Optical spectra of $ZnGeN_2$ grown on sapphire substrate*. 2002.

27. Zhu, L.D., P.E. Norris, and L.O. Bouthillette, *Electronic Bandgap and Refractive Index Dispersion of Single Crystalline Epitaxial $ZnGeN_2$.* Mat. Res. Soc. Symp. Proc., 2000. **607**: p. 291-296.

28. Zhang, Q.H., et al., *Structure, composition, morphology, photoluminescence and cathodoluminescence properties of $ZnGeN_2$ and $ZnGeN_2:Mn^{2+}$ for field emission displays.* Acta Materialia, 2010. **58**: p. 6728-6735.

29. Bekele, C., *Synthesis and Characterization of GaN and $ZnGeN_2$*. 2007.

30. Wu, J., et al., *Unusual properties of the fundamental band gap of InN.* Applied Physics Letters, 2002. **80**(21): p. 3967-3969.

31. Shing, A.M., et al., *Semiconducting $ZnSn_xGe_{1-x}N_2$ alloys prepared by reactive radio-frequency sputtering.* APL Materials, 2015. **3**: p. 076104.

32. Chen, S., et al., *Phase stability and defect physics of a ternary $ZnSnN_2$ semiconductor: first principles insights.* Adv Mater, 2014. **26**: p. 311-315.

33. Zhang, Y., et al., *Effect of Grain Boundary Scattering on Electron Mobility of N-Polarity InN Films.* Applied Physics Express, 2013. **6**: p. 021001.

34. Guo, Q.X., et al., *Observation of visible luminescence from indium nitride at room temperature.* Applied Physics Letters, 2005. **86**(23): p. 231913.

35. Lu, H., et al., *Surface charge accumulation of InN films grown by molecular-beam epitaxy.* Applied Physics Letters, 2003. **82**(11): p. 1736.

36. Cole, D. and J.G. Lunney, *GaN thin films deposited by pulsed laser ablation in nitrogen and ammonia reactive atmospheres.* Mat. Sci. Eng. B-Solid, 1997. **50**: p. 20-24.